nature communications

Article

https://doi.org/10.1038/s41467-025-55939-2

Inhibited peroxidase activity of peroxiredoxin 1 by palmitic acid exacerbates nonalcoholic steatohepatitis in male mice

Received: 21 July 2022

Accepted: 6 January 2025

Published online: 11 January 2025

Check for updates

Wen Yin[1,11], Heng Xu[2,3,11], Zhonghao Bai[1,4,11], Yue Wu[3,5,11], Yan Zhang[1,11], Rui Liu[1], Zhangzhao Wang[1], Bei Zhang[3,5], Jing Shen[1], Hao Zhang[2,3], Xin Chen[6], Danting Ma[1], Xiaofeng Shi[1], Lihui Yan[1], Chang Zhang[7], Hualiang Jiang[3], Kaixian Chen[3], Dean Guo[3], Wenyan Niu[4], Huiyong Yin[6,8,9], Weiping J. Zhang[1], Cheng Luo[2,3,5,10] ✉ & Xiangyang Xie[1] ✉

Reactive oxygen species exacerbate nonalcoholic steatohepatitis (NASH) by oxidizing macromolecules; yet how they promote NASH remains poorly understood. Here, we show that peroxidase activity of global hepatic peroxiredoxin (PRDX) is significantly decreased in NASH, and palmitic acid (PA) binds to PRDX1 and inhibits its peroxidase activity. Using three genetic models, we demonstrate that hepatic PRDX1 protects against NASH in male mice. Mechanistically, PRDX1 suppresses STAT signaling and protects mitochondrial function by scavenging hydrogen peroxide, and mitigating the oxidation of protein tyrosine phosphatases and lipid peroxidation. We further identify rosmarinic acid (RA) as a potent agonist of PRDX1. As revealed by the complex crystal structure, RA binds to PRDX1 and stabilizes its peroxidatic cysteine. RA alleviates NASH through specifically activating PRDX1's peroxidase activity. Thus, beyond revealing the molecular mechanism underlying PA promoting oxidative stress and NASH, our study suggests that boosting PRDX1's peroxidase activity is a promising intervention for treating NASH.

Nonalcoholic fatty liver disease (NAFLD), defined as ectopic lipid accumulation in hepatocytes without excessive alcohol consumption and other causes like viral infections or drug abuse[1], is the most prevalent liver disease worldwide[2] and essentially composed of two forms: non-progressive form with simple steatosis and progressive form (nonalcoholic steatohepatitis, NASH) that may advance to fibrosis, cirrhosis and hepatocellular carcinoma (HCC)[3]. NASH is mostly characterized by steatosis, oxidative stress, inflammation, and hepatocyte ballooning with varying degrees of fibrosis[3], and has emerged as a risk factor of cardiovascular disease and type 2 diabetes (T2D)[4,5]. The

[1]NHC Key Laboratory of Hormones and Development, Tianjin Key Laboratory of Metabolic Diseases, The province and ministry co-sponsored collaborative innovation center for medical epigenetics, Chu Hsien-I Memorial Hospital & Tianjin Institute of Endocrinology, Tianjin Medical University, Tianjin 300134, China. [2]School of Pharmaceutical Science and Technology, Hangzhou Institute for Advanced Study, University of Chinese Academy of Sciences, Hangzhou 310000, China. [3]State Key Laboratory of Drug Research, Shanghai Institute of Materia Medica, Chinese Academy of Sciences, Shanghai 201203, China. [4]Department of Immunology, Key Laboratory of Immune Microenvironment and Disease (Ministry of Education), NHC Key Laboratory of Hormones and Development, Tianjin Medical University, Tianjin 300070, China. [5]University of Chinese Academy of Sciences, 19 Yuquan Road, Beijing 100049, China. [6]CAS Key Laboratory of Nutrition, Metabolism and Food Safety Research, Shanghai Institute of Nutrition and Health (SINH), Chinese Academy of Sciences (CAS), Shanghai, China. [7]Department of Pharmacy, General Hospital, Tianjin Medical University, Tianjin 300070, China. [8]School of Life Science and Technology, ShanghaiTech University, Shanghai, China. [9]Department of Biomedical Sciences, City University of Hong Kong, Hong Kong SAR, China. [10]School of Pharmaceutical Sciences, Zhejiang Chinese Medical University, Hangzhou 310053, China. [11]These authors contributed equally: Wen Yin, Heng Xu, Zhonghao Bai, Yue Wu, Yan Zhang. ✉e-mail: cluo@simm.ac.cn; xyxie@tmu.edu.cn

pathogenesis of NASH is complex and still under debate with different hypotheses[6–8]. Among various pathogenic factors, oxidative stress plays an essential part in NASH[3,8,9]. For instance, oxidative stress is involved in NASH pathogenesis through boosting inflammation[7]. Hydrogen peroxide (H_2O_2) activates nuclear factor kappa B (NF-κB) and stimulates the inflammatory response[10]. Increased reactive oxygen species (ROS) and the resultant lipid peroxidation promote the inflammatory response[6]. Although hepatocyte ROS have been shown to profoundly promote NASH and liver fibrosis[3,11,12], how they are controlled remains to be elucidated.

Oxidative stress was initially defined as an imbalance between pro-oxidant and anti-oxidant favoring the former; however, in the past decades, this definition has been redefined and now includes the transfer of oxidizing equivalents from a peroxidase to another target protein that is known as 'redox relay'[13,14]. Thus, oxidative stress exerts a tremendous impact both physiologically and pathologically[13]. The anti-oxidant system consists of non-enzymatic and enzymatic anti-oxidants including superoxide dismutase (SOD), catalase, glutathione peroxidase, and peroxiredoxin (PRDX)[13,15]. A protective role for anti-oxidants in NASH has been implicated in one study showing reduced glutathione and activities of catalase and SOD in NASH patients[16]. The mammalian PRDX family is composed of six peroxidases and guards against oxidative stress by scavenging the majority of intracellular peroxides[17–20]. Of interest, numerous studies have demonstrated that PRDX1 is involved in a variety of intracellular events and human diseases by functioning as either a peroxidase or a chaperone[17,18,21–27]. On one hand, PRDX1 has been shown to protect against alcohol-induced liver injury through its peroxidase activity[27], or alleviate inflammation and NASH through its chaperone activity[25,26]. On the other hand, PRDX1 also has been suggested to promote inflammation and aggravate liver injury through its chaperone activity[23,24]. Thus far, the functional role of PRDX1 in NASH through its peroxidase activity remains poorly understood.

In this study, we show that the peroxidase activity of global hepatic PRDX is significantly decreased in NASH mouse models. Palmitic acid directly binds to PRDX1 and reduces its peroxidase activity. We demonstrate that hepatic PRDX1 protects against NASH through three mouse models. By scavenging H_2O_2 and mitigating the oxidation of protein tyrosine phosphatases and lipid peroxidation, PRDX1 suppresses STAT1 and STAT3 signaling and protects liver mitochondrial function. Finally, we identify rosmarinic acid (RA) as a potent agonist of PRDX1 with a dissociation constant at nanomolar levels. As revealed by the complex crystal structure, RA binds to PRDX1 and stabilizes its peroxidation cysteine. RA treatment in WT mice alleviates NASH and fibrosis, while it loses these beneficial effects in PRDX1 knockout mice. Thus, boosting PRDX1's peroxidase activity is a promising therapeutic intervention for NASH.

Results

Decreased peroxidase activity of global hepatic PRDX in NASH

To examine whether the global PRDX peroxidase activity in the liver was altered in NASH, we applied a classic Trx-TrxR-NADPH coupled assay[28,29] where PRDX peroxidase activity is coupled to NADPH oxidation via thioredoxin (Trx) and thioredoxin reductase (TrxR), and accordingly can be evaluated indirectly by measuring NADPH consumption rates (Supplementary Fig. 1a). Given that the majority of intracellular peroxides are thought to be quenched by PRDX family members[18], the Trx-TrxR-NADPH coupled assay can be applied to measure the global PRDX peroxidase activity. Using this assay, we compared the global hepatic PRDX peroxidase activity in various NASH mouse models induced by special diets with that in mice fed a normal chow (NC) diet. High-fat diet (HFD) feeding for 18 weeks significantly increased serum aspartate aminotransferase (AST) and alanine aminotransferase (ALT) levels, which are indicative of liver injury[30] (Supplementary Fig. 1b), and hepatic H_2O_2 levels that were revealed by staining of HKPerox-Red, a selective H_2O_2 probe[31] (Supplementary Fig. 1c).

As demonstrated by the reduced NADPH consumption rates, HFD significantly decreased the global PRDX peroxidase activity in the liver (Fig. 1a). HFD did not alter the protein levels of most PRDX family enzymes, but significantly increased PRDX4 protein levels in the liver (Fig. 1b). Interestingly, previous studies have demonstrated that exposure to H_2O_2 can hyperoxidize some PRDX members (PRDX1-PRDX3) at their active cysteine to form sulfinic acid (SO2) or sulfonic acid (SO3)[17]. Of note, formation of PRDX-SO2 causes a reversible inactivation of PRDX peroxidase activity[32], while formation of PRDX-SO3 causes an irreversible inactivation of PRDX peroxidase activity. Thus, we used an antibody (Anti-Peroxiredoxin-SO3, ab16830, abcam) that recognizes both SO2 and SO3 forms of PRDX[33] to detect PRDX hyperoxidation. Our observation of no difference in the extent of hepatic PRDX hyperoxidation between NC and HFD groups (Supplementary Fig. 1d) excluded that the observed decrease in the global PRDX peroxidase activity after HFD results from hyperoxidation.

We also assessed the global PRDX peroxidase activity in the liver in two additional common experimental models of NASH, including NASH with obesity induced by a western diet (WD) that is rich in fat, fructose, and cholesterol, and NASH without obesity induced by a methionine and choline deficient diet (MCD)[7]. WD feeding (20 weeks) significantly decreased the global hepatic PRDX peroxidase activity and protein levels of PRDX1 and PRDX4, but increased PRDX3 levels in the liver (Fig. 1c, d). WD significantly increased hepatic H_2O_2 levels as shown by HKPerox-Red staining (Supplementary Fig. 1e), and hepatic levels of hepatic malondialdehyde (MDA) (Supplementary Fig. 1f), a marker for lipid peroxidation[9], and serum levels of ALT and AST (Supplementary Fig. 1g). WD feeding did not affect the extent of hepatic PRDX hyperoxidation (Supplementary Fig.1h). We also observed that MCD feeding (5 weeks) significantly reduced the global PRDX peroxidase activity in the liver (Fig. 1e) and protein levels of PRDX1, PRDX5, and PRDX6, but significantly increased PRDX3 levels in the liver (Fig. 1f). MCD significantly increased hepatic H_2O_2 levels (Supplementary Fig. 1i), and hepatic levels of hepatic MDA (Supplementary Fig. 1j) and serum levels of ALT and AST (Supplementary Fig. 1k). MCD feeding had no effect on the extent of hepatic PRDX hyperoxidation as indicated (Supplementary Fig. 1l). Collectively, these results establish that the global PRDX peroxidase activity in the liver is reduced in NASH, and suggest that decreased PRDX peroxidase activity contributes to hepatic oxidative stress and NASH pathogenesis.

PA binds to PRDX1 and inhibits its peroxidase activity

We next investigated potential causes of the decreased PRDX peroxidase activity in NASH. Free fatty acids (FFA) and pro-inflammatory cytokines such as interleukin 6 (IL-6) and interferons are elevated in NASH[3,34]. PA is the most common and abundant saturated FFA with potent toxic effects on promoting NASH[35]. PA treatment (1 hr) in HepG2 cells significantly decreased the global PRDX peroxidase activity and increased the intracellular ROS levels (Fig. 2a, b). In addition, treatment with PA at higher concentration of (500 μM vs 250 μM) significantly increased H_2O_2 levels in HepG2 cells (Fig. 2c, d). Of note, PA treatment did not alter PRDX protein levels (Supplementary Fig. 2a), or the extent of PRDX hyperoxidation (Supplementary Fig. 2b), supporting that the observed decrease in the global PRDX peroxidase activity is directly induced by PA treatment.

To test whether PA directly binds to PRDX1, we performed the surface plasmon resonance (SPR) assay, where sodium palmitate was used due to a poor solubility of PA. Sodium palmitate directly bound to recombinant WT PRDX1, yielding a dissociation constant (K_D) of 75.3 ± 4.5 μM (Fig. 2e). Using the cellular thermal shift assay[36], we also observed the significantly increased thermal stabilization of PRDX1 upon PA binding in HepG2 cells (Fig. 2f). We further evaluated the

https://doi.org/10.1038/s41467-025-55939-2

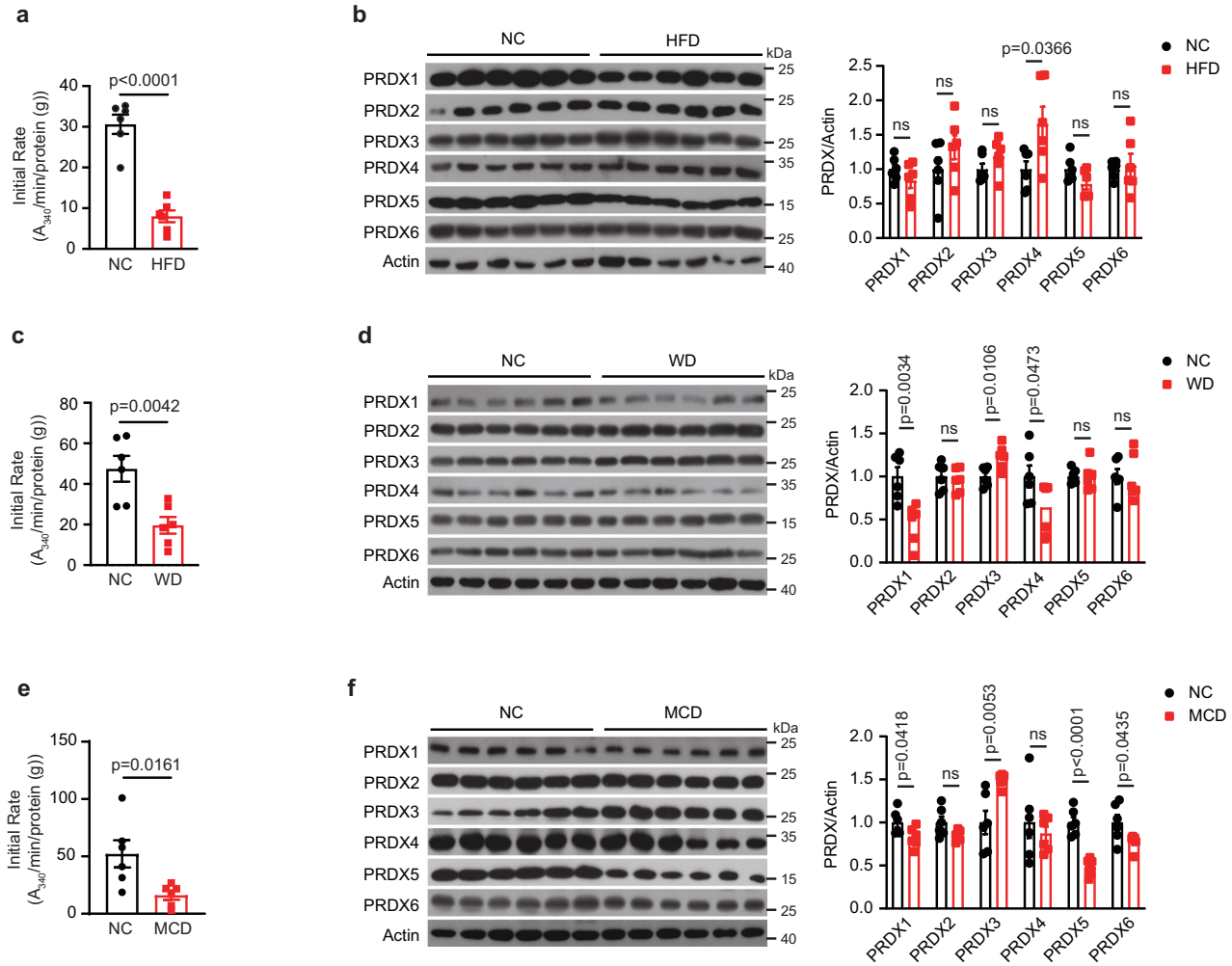

Fig. 1 | Decreased peroxidase activity of global hepatic PRDX in NASH. **a** Peroxidase activity of global hepatic PRDX after normal chow (NC) or high-fat diet (HFD) feeding. 8-week-old male C57BL/6 mice were fed a NC or HFD for 18 weeks and liver samples were collected for biochemical analyses. Global hepatic PRDX peroxidase activity was measured using a classic Trx-TrxR-NADPH coupled assay. NADPH consumption was monitored via absorbance at 340 nm (A_{340}) in 15 min assay duration. Meanwhile, the background activity was assessed without Trx and TrxR, but only with H_2O_2 and NADPH. To calculate the initial NADPH consumption rate (initial rate) (A_{340}/min/protein (g)) in the first 5 min, a smooth curve was drawn through A_{340} readings, and the initial rate was calculated by performing a simple linear regression. Global PRDX peroxidase activity was calculated by subtracting the background activity (initial rate) from total activity (initial rate). $n = 6$ mice per group. **b** Protein levels of hepatic PRDX family enzymes after HFD (as in a) and quantitation. $n = 6$ mice per group; ns, no significance. **c** Peroxidase activity of global hepatic PRDX after NC or western diet (WD). 8-week-old male C57BL/6 mice were fed a NC or WD for 20 weeks and global hepatic PRDX peroxidase activity was measured using a classic Trx-TrxR-NADPH coupled assay. $n = 6$ mice per group. **d** Protein levels of hepatic PRDX family enzymes after NC or WD feeding (as in c) and quantitation. $n = 6$ mice per group; ns, no significance. **e** Peroxidase activity of global hepatic PRDX after NC or methionine and choline deficient diet (MCD). 8-week-old male C57BL/6 mice were fed a NC or MCD for 5 weeks and global hepatic PRDX peroxidase activity was measured using a classic Trx-TrxR-NADPH coupled assay. $n = 6$ mice per group. **f** Protein levels of hepatic PRDX family enzymes after NC or MCD feeding (as in e) and quantitation. $n = 6$ mice per group; ns, no significance. All data are presented as means ± SEM. Unpaired and two-tailed Student's t test was performed for **a**–**f**.

effect of sodium palmitate on recombinant WT PRDX1's peroxidase activity though the Trx-TrxR-NADPH assay. Sodium palmitate inhibited PRDX1's peroxidase activity in a dose dependent manner, with a maximal inhibition rate at 46.6% (Fig. 2g).

To further evaluate the in vivo role of PA in NASH pathogenesis, we fed mice a choline-deficient, amino acid-defined, HFD (CDAHFD) (another common diet to induce NASH[37]) that contains different amounts of PA (10% PA vs 20% PA) but same energy density (Supplementary Table 3)[38]. High PA CDAHFD did not change body weight, but significantly increased liver weight, serum levels of ALT, AST and TG, and hepatic MDA contents (Supplementary Fig. 2c–g). In addition, high PA CDAHFD significantly reduced the global hepatic PRDX peroxidase activity, compared with low PA CDAHFD and NC groups (Supplementary Fig. 2h). Histologically, we observed more severe phenotypes of NASH and liver fibrosis in high PA CDAHFD-fed mice than low PA CDAHFD-fed mice, as assessed by staining of hematoxylin and eosin (H&E), Oil Red O, and smooth muscle actin alpha (α-SMA) (Supplementary Fig. 2i). Collectively, these results suggest that PA promotes NASH by inhibiting PRDX1's peroxidase activity and increasing oxidative stress.

PRDX1 knockout exacerbates NASH and liver fibrosis

To investigate potential impacts of PRDX1 in NASH pathogenesis, we generated a PRDX1 knockout (*Prdx1*$^{-/-}$) mouse strain (Fig. 3a), and observed the significantly reduced peroxidase activity of global hepatic PRDX in *Prdx1*$^{-/-}$ mice (Fig. 3b). After 6 weeks of WD feeding, *Prdx1*$^{-/-}$ mice had significantly higher body weights than their wild-type (WT) littermates (Fig. 3c). Note that there was no difference of food intake between WT and *Prdx1*$^{-/-}$ mice (Fig. 3d), suggesting that increased body weight of *Prdx1*$^{-/-}$ mice could be owing to decreased

https://doi.org/10.1038/s41467-025-55939-2

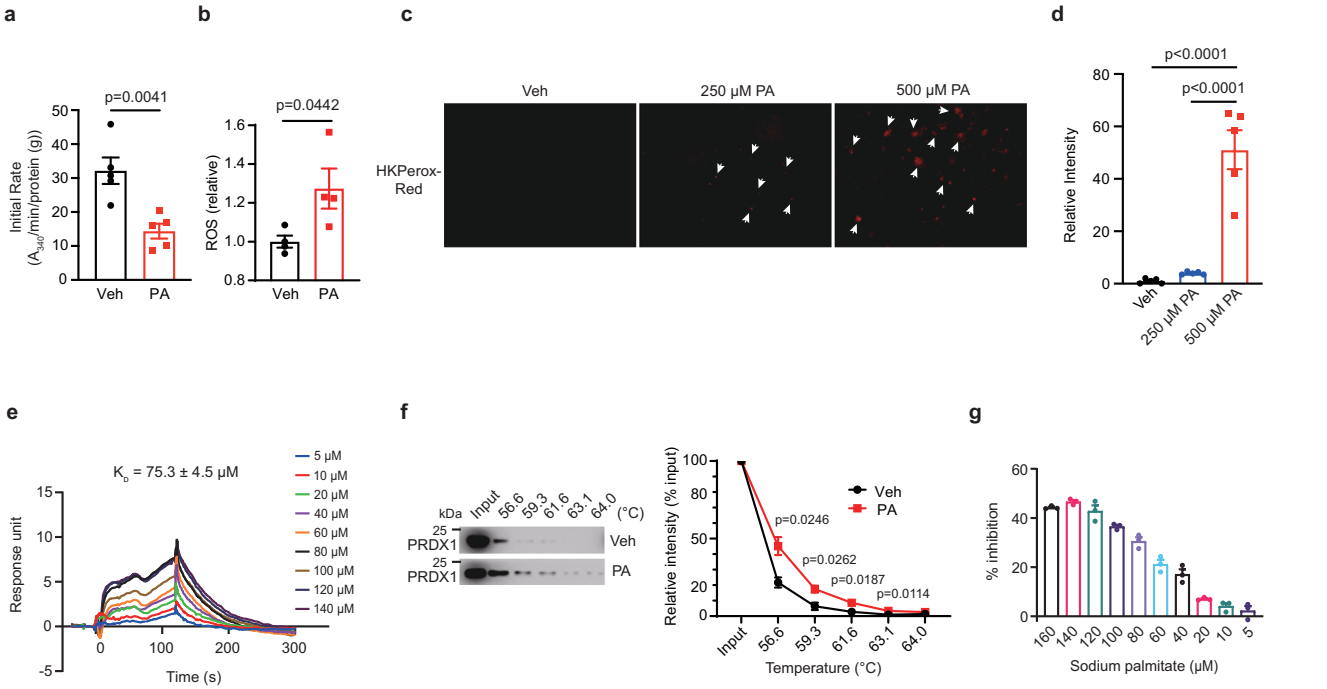

Fig. 2 | PA binds to PRDX1 and inhibits its peroxidase activity. a Global PRDX peroxidase activity in HepG2 cells after PA (250 μM) treatment for 1 hr. Veh, vehicle. PA, palmitic acid. $n = 5$ biologically independent samples. **b** ROS levels in HepG2 cells after PA treatment for 1 hr. Intracellular ROS were monitored by measuring the fluorescent intensity of dichlorofluorescin (DCF) using a fluorometer. $n = 4$ independent experiments. **c** Representative images of HKPerox-Red staining in HepG2 cells after treatment with Veh or PA at different concentrations for 1 hr. Arrows denote the signals of HKPerox-Red staining. $n = 5$ independent experiments. Scale bar, 50 μm. **d** Quantification of fluorescence intensity of images from c. $n = 5$ independent experiments. **e** Binding affinity of sodium palmitate on recombinant PRDX1 determined by SPR assay. Data were calculated from three independent experiments. **f** Representative images showing the increased thermal stabilization of PRDX1 after binding to PA and quantification. $n = 3$ independent experiments. HepG2 cells were treated with PA (250 μM) for 1 hr and then the cell lysate was collected for the thermal shift assay. In brief, the cell lysate was divided into six aliquots. One aliquot was used for input control and the other five aliquots were heated at different temperatures as indicated for 3 min. Finally, western blotting was carried out to detect PRDX1 stability. **g** Inhibition of recombinant WT PRDX1's peroxidase activity by sodium palmitate at different concentrations as indicated. For more details, please see methods section. Data were calculated from three independent experiments. All the data are presented as means ± SEM. Unpaired and two-tailed Student's t test was performed for **a, b, d**, and **f**.

energy expenditure. Compared with WT mice, *Prdx1*$^{-/-}$ mice exhibited significantly decreased insulin sensitivity, as assessed with intraperitoneal glucose tolerance test (IPGTT) and intraperitoneal insulin tolerance test (IPITT) (Fig. 3e, f), as well as significantly increased serum ALT and AST levels (Fig. 3g). *Prdx1*$^{-/-}$ mice showed significantly increased hepatic H_2O_2 levels, fat accumulation, and liver fibrosis as assessed by staining of HKPerox-Red, H&E, Oil Red O, Sirius Red, and α-SMA (Fig. 3h–j).

To test whether hepatic PRDX1 confers protection against NASH, we generated floxed Prdx1 (*Prdx1*$^{fl/fl}$) mice (Supplementary Fig. 3a), and crossed them with Albumin-Cre mice[39] (Alb-Cre;*Prdx1*$^{fl/fl}$) to delete Prdx1 specifically from the liver (Supplementary Fig. 3b). The peroxidase activity of global hepatic PRDX was significantly reduced in *Alb-Cre;Prdx1*$^{fl/fl}$ mice (Supplementary Fig. 3c).

When fed a WD (20 weeks), *Alb-Cre;Prdx1*$^{fl/fl}$ mice showed no differences from *Prdx1*$^{fl/fl}$ control mice in body weight (Supplementary Fig. 3d), food intake (Supplementary Fig. 3e), energy expenditure (Supplementary Fig. 3f), and insulin sensitivity (Supplementary Fig. 3g, h), but they uniquely increased steatosis and liver fibrosis (Supplementary Fig. 3i, j). In agreement with these phenotypes, the expression of several hepatic genes related to inflammation and fibrosis (*e.g.*, *Cd11b*, *Col1a1*, *Col3a1*, *Pdgfb*, and *Pdgfra*) was significantly increased in *Alb-Cre;Prdx1*$^{fl/fl}$ mice (Supplementary Fig. 3k).

When fed a MCD (5 weeks), *Alb-Cre;Prdx1*$^{fl/fl}$ mice showed similar hepatic fat accumulation to *Prdx1*$^{fl/fl}$ control mice (Supplementary Fig. 3i), but exhibited severe liver fibrosis (Supplementary Fig. 3m), and significantly increased the expression levels of inflammatory or fibrotic genes (*e.g*, *F4/80*, *Col3a1*, *Pdgfb*, and *Pdgfra*) in the liver (Supplementary Fig. 3n). We also observed significant increases in H_2O_2 levels and the extent of lipid peroxidation in the liver of *Alb-Cre;Prdx1*$^{fl/fl}$ mice (Supplementary Fig. 3o, p). Collectively, these results demonstrate that PRDX1 knockout exacerbates NASH and liver fibrosis.

PRDX1 overexpression ameliorates NASH and liver fibrosis

To further understand how PRDX1 influences NASH, we made a PRDX1 overexpression (*Prdx1*$^{OE/OE}$) mouse line (Supplementary Fig. 4a, b). *Prdx1*$^{OE/OE}$ mice showed significantly increased peroxidase activity of global hepatic PRDX (Fig. 4a).

After 8 weeks of WD feeding, *Prdx1*$^{OE/OE}$ mice had significantly less body weights (Fig. 4b) but no difference in food intake than WT mice (Fig. 4c), suggesting increased energy expenditure in *Prdx1*$^{OE/OE}$ mice. Indeed, *Prdx1*$^{OE/OE}$ mice showed significantly increased energy expenditure at night time (Fig. 4d), but similar locomotion activity compared with WT mice (Fig. 4e). *Prdx1*$^{OE/OE}$ mice showed significantly improved insulin sensitivity, as demonstrated by lower fasting glucose levels and significantly improved insulin tolerance compared to WT mice (Fig. 4f, g), and showed significant reductions in serum ALT and AST levels (Fig. 4h), hepatic H_2O_2 levels (Fig. 4i, and Supplementary Fig. 4c), and the extent of hepatic lipid peroxidation (Fig. 4j). In addition, lipid accumulation and fibrosis in the liver were markedly reduced in *Prdx1*$^{OE/OE}$ mice compared to WT mice (Fig. 4k, l). In line with these phenotypes, numerous pro-inflammatory or fibrotic genes (*e.g.*, *Mcp-1*, *F4/80*, *Cd11b*, *Tnf-α*, *Il-6*, *Col1a1*, *Col3a1*, *Pdgfa* and *Pdgfra*) were significantly downregulated in the livers of *Prdx1*$^{OE/OE}$ mice (Fig. 4m).

https://doi.org/10.1038/s41467-025-55939-2

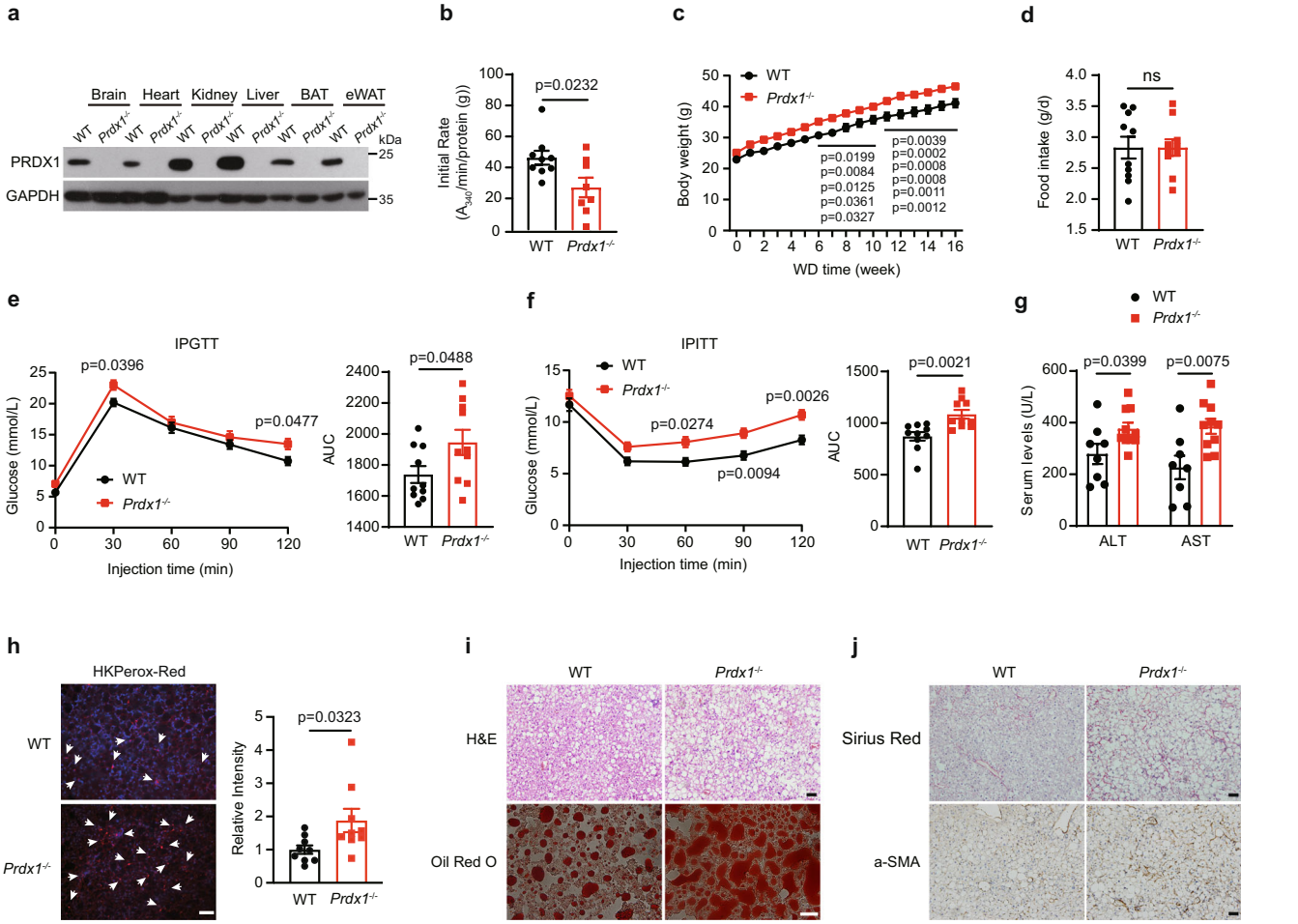

Fig. 3 | PRDX1 knockout increases NASH and liver fibrosis. a Representative images validating the efficiency of PRDX1 knockout in *Prdx1*$^{-/-}$ mice. This experiment was repeated for three times independently. **b** Peroxidase activity of global hepatic PRDX in WT and *Prdx1*$^{-/-}$ mice. WT mice ($n = 9$); *Prdx1*$^{-/-}$ mice ($n = 8$). **c** Body weight of WT and *Prdx1*$^{-/-}$ mice on WD. 8-week-old male mice were fed a WD for 20 weeks and their weekly body weights were monitored. $n = 10$ mice per group. **d** Daily food intake of mice on WD (as in **c**). $n = 10$ mice per group; ns, no significance. **e** Intraperitoneal glucose tolerance test (IPGTT) in mice on WD (as in **c**) and area under the curve (AUC). $n = 10$ mice per group. **f** Intraperitoneal insulin tolerance test (IPITT) in mice on WD (as in **c**) and AUC. $n = 10$ mice per group. **g** Circulating ALT and AST levels (as in **c**). WT mice ($n = 8$); *Prdx1*$^{-/-}$ mice ($n = 10$). **h** Representative images of HKperox-Red staining in the liver and quantitative analysis (as in **c**). Arrows denote the signals of HKPerox-Red staining. Scale bar, 50 μm. $n = 9$ images from three mice per group. **i** Representative images showing H&E and Oil Red O staining in the liver after WD (as in **c**). $n = 3$ biologically independent mice. Scale bars, 50 μm. **j** Representative images showing Sirius Red and α-SMA staining in the liver (as in **c**). $n = 3$ biologically independent mice. Scale bars, 50 μm. All data are presented as means ± SEM. Unpaired and two-tailed Student's t test was performed for **b, d**, AUC of **e**, AUC of **f, g**, and **h**. Two-way ANOVA followed by Bonferroni's test for multiple comparisons was performed for **c, e**, and **f**.

When fed a MCD, *Prdx1*$^{OE/OE}$ mice showed similar body weight (Supplementary Fig. 4d), and fat accumulation in the liver (Supplementary Fig. 4e), but significantly reduced liver fibrosis (Supplementary Fig. 4f), the levels of hepatic H_2O_2 and MDA (Supplementary Fig. 4g, h), and the expression of hepatic pro-inflammatory and fibrotic genes (*Mcp-1, Il-1b, Col1a1*, and *Col3a1)* (Supplementary Fig. 4i). Together, these results demonstrate that PRDX1 overexpression protects against NASH and liver fibrosis.

PRDX1 suppresses hepatic STAT1 and STAT3 signaling

Protein tyrosine phosphatases (PTPs) inhibit JAK-STAT signaling[40]. Previous studies have shown that obesity-associated ROS oxidize and inactivate PTPs (e.g., PTP1B and T cell protein tyrosine phosphatase (TCPTP)), consequently increasing hepatic STAT signaling and promoting NAFLD[41,42]. Consistently, we observed that hepatic PTPs' oxidation (Fig. 5a, b), and hepatic STAT1 and STAT3 phosphorylation (Fig. 5c, d) were drastically increased in both WD- and MCD-induced NASH mouse models. Further, H_2O_2 treatment (30 min) in HepG2 cells dose-dependently increased PTPs' oxidization (Supplementary Fig. 5a), and STAT1 and STAT3 phosphorylation (Supplementary Fig. 5b). Together, these results suggest that by oxidizing and inactivating PTPs, H_2O_2 increases STAT signaling and promotes NASH.

IL-6 and IFN-γ are known to stimulate STAT signaling[43]. We questioned if increased H_2O_2 levels promote IL-6- and IFN-γ-stimulated STAT signaling. Interestingly, treatment with either IL-6- or IFN-γ in HepG2 cells significantly increased intracellular H_2O_2 levels (Supplementary Fig. 5c, d), and phosphorylation of STAT1 and STAT3 (Supplementary Fig. 5e, f), which were drastically reduced by pretreatment with a potent anti-oxidant (N-acetylcysteine (NAC))[44].

To study how PRDX1 regulates STAT signaling, we generated PRDX1 knockout HepG2 cells (Supplementary Fig. 5g), which showed significantly reduced global PRDX peroxidase activity (Supplementary Fig. 5h), and significantly increased intracellular H_2O_2 levels as well as extent of lipid peroxidation (Supplementary Fig. 5i–k). In addition, the oxidation of PTPs (Supplementary Fig. 5l), and IL-6- or IFN-γ-induced phosphorylation of STAT1 and STAT3 (Supplementary Fig. 5m, n), all were drastically increased in PRDX1 knockout HepG2 cells compared to WT HepG2 cells. Consistently, PRDX1 knockout significantly increased hepatic STAT1 and STAT3 phosphorylation in MCD- and WD-induced NASH (Fig. 5e, f, and Supplementary Fig. 5o). In contrast,

https://doi.org/10.1038/s41467-025-55939-2

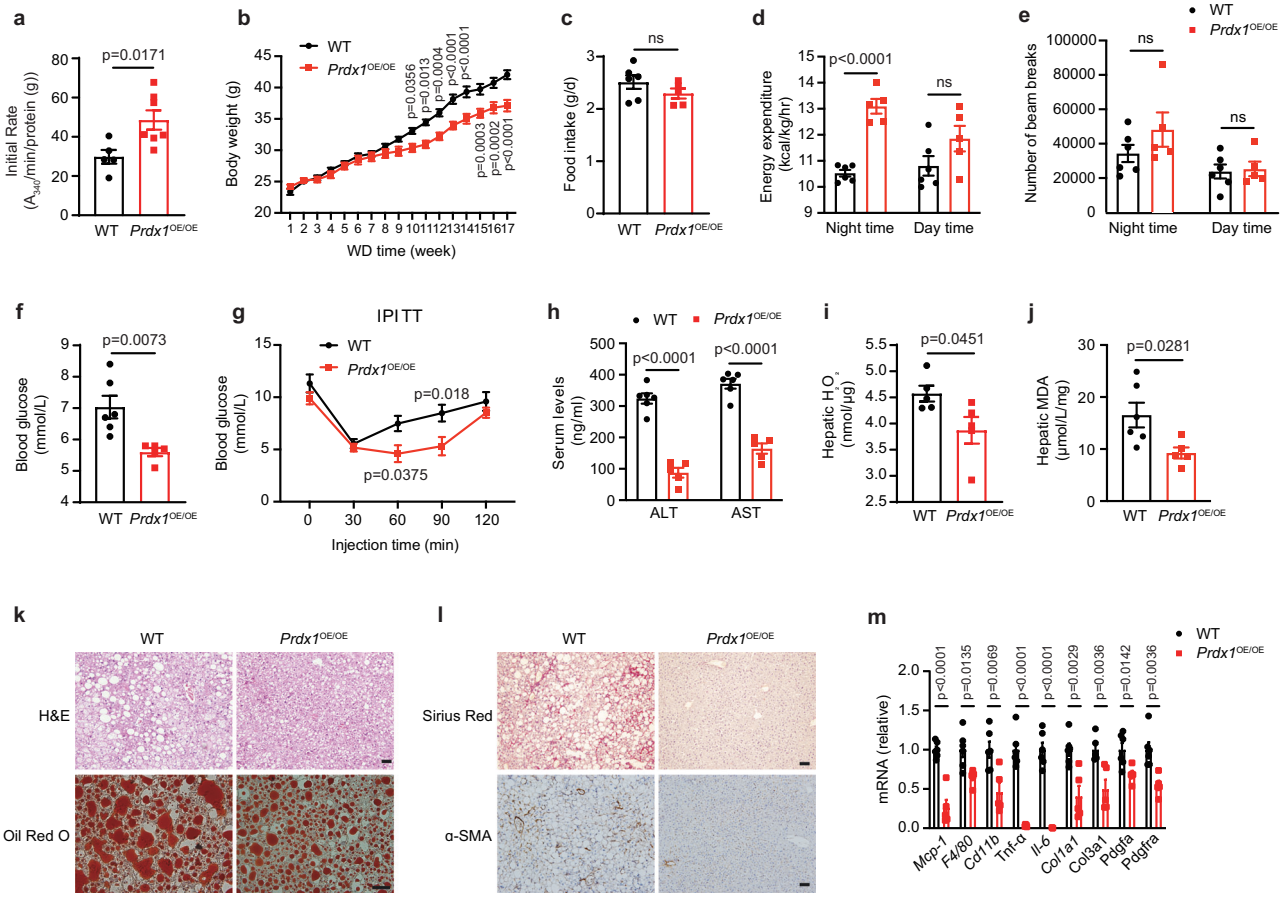

Fig. 4 | PRDX1 overexpression ameliorates NASH and liver fibrosis. a Peroxidase activity of global hepatic PRDX in WT and *Prdx1*$^{OE/OE}$ mice. WT mice ($n = 5$); *Prdx1*$^{OE/OE}$ mice ($n = 7$). **b** Body weight of WT and *Prdx1*$^{OE/OE}$ mice on WD. 8-week-old male mice were fed a WD and their body weights were monitored weekly. WT mice ($n = 6$); *Prdx1*$^{OE/OE}$ mice ($n = 5$). **c** Daily food intake of mice on WD (as in b). WT mice ($n = 6$); *Prdx1*$^{OE/OE}$ mice ($n = 5$). ns, no significance. **d** Energy expenditure (kcal) of mice on WD (as in b). WT mice ($n = 6$); *Prdx1*$^{OE/OE}$ mice ($n = 5$). **e** Locomotion activity of mice on WD (as in b). WT mice ($n = 6$); *Prdx1*$^{OE/OE}$ mice ($n = 5$). ns, no significance. **f** Fasting blood glucose levels of mice on WD (as in b). WT mice ($n = 6$); *Prdx1*$^{OE/OE}$ mice ($n = 5$). **g** IPITT in mice on WD (as in b). WT mice ($n = 6$); *Prdx1*$^{OE/OE}$ mice ($n = 5$). **h** Serum ALT and AST levels in mice on WD (as in b). WT mice ($n = 6$); *Prdx1*$^{OE/OE}$ mice ($n = 5$). **i** Hepatic H_2O_2 levels in WD-fed mice (as in b). $n = 5$ mice per group. **j** Hepatic MDA levels in WD-fed WT and *Prdx1*$^{OE/OE}$ mice (as in b). WT mice ($n = 6$); *Prdx1*$^{OE/OE}$ mice ($n = 5$). **k** Representative images showing H&E and Oil Red O staining of liver after WD (as in b). $n = 3$ biologically independent mice. Scale bars, 50 μm. **l** Representative images from three mice per group showing Sirius Red and α-SMA staining of liver after WD (as in b). $n = 3$ biologically independent mice. Scale bars, 50 μm. **m** mRNA expression of hepatic genes after WD (as in b). WT mice ($n = 6$); *Prdx1*$^{OE/OE}$ mice ($n = 5$). All the data are presented as means ± SEM. Unpaired and two-tailed Student's t test was performed for **a**, **c**, **d**, **e**, **f**, **h**, **i**, **j**, and **m**. Two-way ANOVA followed by Bonferroni's test for multiple comparisons was performed for **b** and **g**.

PRDX1 overexpression significantly reduced the phosphorylation of hepatic STAT1 and STAT3 in WD-induced NASH (Fig. 5g). These results collectively indicate that PRDX1 suppresses STAT signaling by scavenging H_2O_2 and mitigating the oxidation of PTPs.

To further support that PRDX1 suppresses STAT signaling, we performed RNA sequencing of liver samples from WT and Alb-Cre;*Prdx1*$^{fl/fl}$ mutant mice fed a MCD. Gene-set enrichment analysis (GSEA) and KEGG pathway enrichment analysis revealed enrichments for genes related to JAK-STAT signaling pathway in Alb-Cre;*Prdx1*$^{fl/fl}$ mutant mice (Supplementary Fig. 6a, b). Intriguingly, the expression of numerous genes in JAK-STAT signaling including some fibrotic genes such as *Pdgfb* and *Pdgfra* was significantly increased in Alb-Cre;*Prdx1*$^{fl/fl}$ mutant mice (Supplementary Fig. 6c).

PRDX1 protects liver mitochondrial function

Liver mitochondrial dysfunction, which could be caused by hepatic lipid peroxidation[45], is a driving force of NASH[46]. Using an Oroboros Oxygraph-2k (O2k) system, one clinical study showed that liver mitochondrial function was compromised in NASH patients with increased hepatic H_2O_2 levels and lipid peroxidation, which mainly was revealed by a significant increase in the leaking control ratio (LCR) and a significant decrease in the respiratory control ratio (RCR)[47].

Using a similar O2k approach, we investigated the function of liver mitochondria isolated from different NASH mouse models. Both WD (20 weeks) and MCD (5 weeks) significantly reduced the RCR (Fig. 6a and Supplementary Fig. 7a) and increased the LCR in the liver mitochondria of WT mice (Fig. 6b and Supplementary Fig. 7b). In addition, citrate synthase activity (CSA) was significantly increased in both NASH models (Fig. 6c and Supplementary Fig. 7c), which is indicative of mitochondrial dysfunction[48]. Of interest, mitochondrial oxygen (O_2) flux (per CSA) was significantly increased in the liver of MCD-fed mice (Supplementary Fig. 7d), while no change of liver mitochondrial O_2 flux was observed in WD-fed mice compared to NC-fed mice (Fig. 6d). We also detected a significant increase in the extent of lipid peroxidation in the liver mitochondria of WD- and MCD-fed mice (Fig. 6e and Supplementary Fig. 7e). These results collectively suggest that lipid peroxidation-induced mitochondrial dysfunction contributes to the development and progression of NASH (with or without obesity).

To test whether PRDX1 protects liver mitochondrial function by mitigating lipid peroxidation, we performed O2k analyses in *Prdx1*$^{OE/OE}$ and WT mice fed a WD (20 weeks) or a MCD (5 weeks) to induce NASH.

https://doi.org/10.1038/s41467-025-55939-2

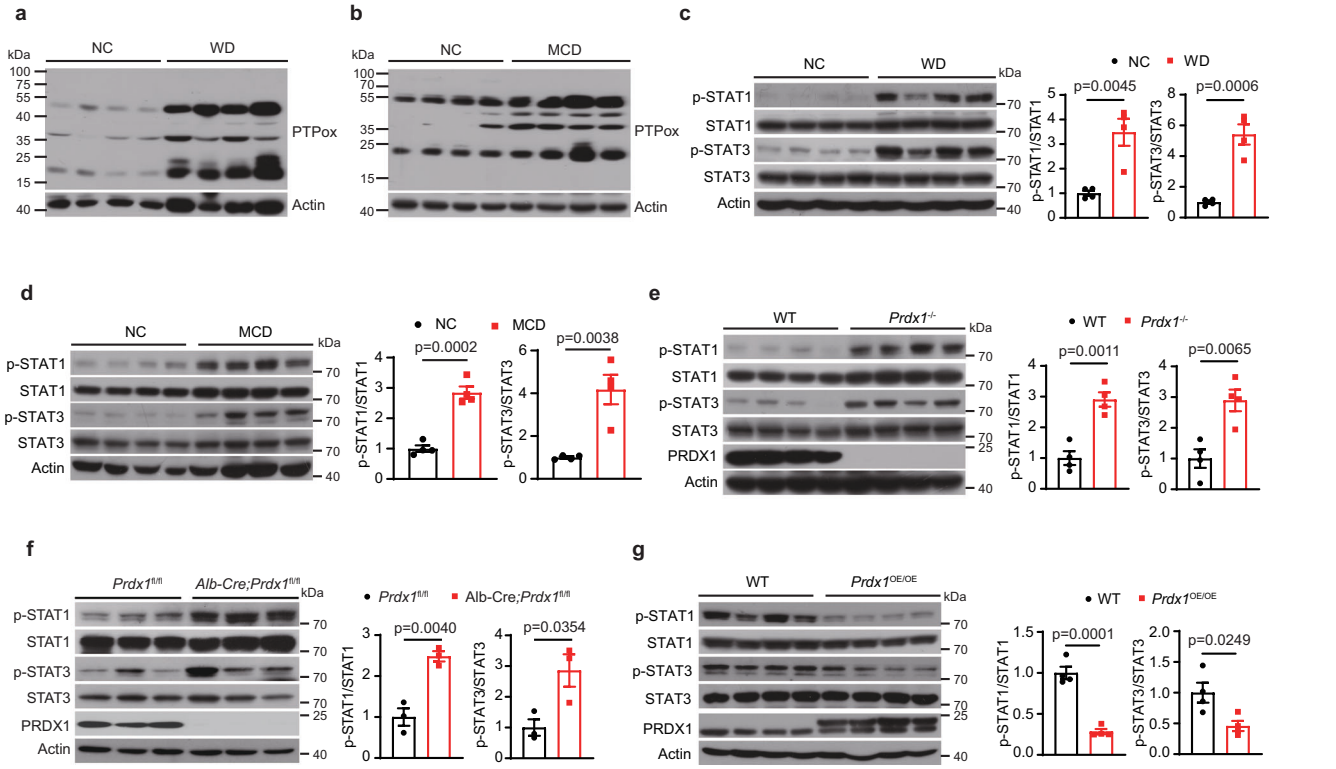

Fig. 5 | PRDX1 suppresses hepatic STAT1 and STAT3 phosphorylation. a Western blotting of the oxidation of hepatic protein tyrosine phosphatases (PTPs) in WT mice after NC or WD for 20 weeks. $n = 4$ mice per group. **b** Western blotting of the oxidation of hepatic PTPs in WT mice after NC or MCD for 2 weeks. $n = 4$ mice per group. **c** Western blotting and quantitation of hepatic STAT1 and STAT3 phosphorylation (as in a). $n = 4$ mice per group. **d** Western blotting and quantitation of hepatic STAT1 and STAT3 phosphorylation (as in b). $n = 4$ mice per group. **e** Western blotting and quantitation of hepatic STAT1 and STAT3 phosphorylation in MCD-fed WT and *Prdx1*$^{-/-}$ mice. $n = 4$ mice per group. **f** Western blotting and quantitation of hepatic STAT1 and STAT3 phosphorylation in WD-fed WT and Alb-Cre;*Prdx1*$^{fl/fl}$ mice. $n = 3$ mice per group. **g** Western blotting and quantitation of hepatic STAT1 and STAT3 phosphorylation in WD-fed WT and *Prdx1*$^{OE/OE}$ mice. $n = 4$ mice per group. All the data are presented as means ± SEM. Unpaired and two-tailed Student's t test was performed for **c**–**g**.

Compared to WT mice, *Prdx1*$^{OE/OE}$ mice showed improved mitochondrial function reflected by significantly increased RCR (Fig. 6f) and significantly decreased LCR (Fig. 6g) after WD feeding. Hepatic CSA tended to be significantly reduced in *Prdx1*$^{OE/OE}$ mice ($p = 0.053$) (Fig. 6h), while no difference in liver mitochondrial O_2 flux was observed between WT and *Prdx1*$^{OE/OE}$ mice (Fig. 6i). In addition, the extent of lipid peroxidation was significantly reduced in liver mitochondria of *Prdx1*$^{OE/OE}$ mice (Fig. 6j).

We also observed a significant increase of RCR (Supplementary Fig. 7f) and a significant decrease of LCR (Supplementary Fig. 7g) in *Prdx1*$^{OE/OE}$ mice compared with WT mice after MCD feeding, although there was no difference in CSA and liver mitochondrial O_2 flux between these two genotypes (Supplementary Fig. 7h, i). Further, lipid peroxidation levels were significantly reduced in the liver mitochondria of *Prdx1*$^{OE/OE}$ mice (Supplementary Fig. 7j). Together, these results support that beyond suppressing STAT signaling, PRDX1 protects liver mitochondrial function by scavenging H_2O_2 and mitigating lipid peroxidation in the liver mitochondria.

Identification of rosmarinic acid as an agonist of PRDX1

Our results collectively suggest that boosting PRDX1's peroxidase activity is a potential way in combating NASH. Through protein thermal shift assay (PTS) based compound library screening and peroxidase activity assay based validation, we identified rosmarinic acid (RA) as a highly active agonist of PRDX1 (Fig. 7a and Supplementary Fig. 8a). The half maximal concentration of RA for activating PRDX1's peroxidase activity is 253.1 ± 49.0 nM (Fig. 7b), while the K_D of RA with PRDX1 is 375.7 ± 2.5 nM as revealed by SPR (Fig. 7c).

As a typical 2-Cys peroxidase, PRDX1 contains a peroxidatic cysteine (C52) and a resolving cysteine (C173)[17]. To better understand the mechanism of PRDX1 activation by RA, we solved a complex structure of RA with PRDX1 variant, PRDX1^{C52SC83S} (aa1-175) (Supplementary Table 1), where both C52 and C83 residues were mutated to serine, and the C-terminus (aa 176-199) of WT PRDX1 protein was truncated, given that only PRDX1^{C52SC83S} (aa1-175) variant could achieve repeatable and high-resolution crystals after crystallization screening with WT and different PRDX1 variants. F_O-F_C (Fig. 7d) and 2F_O-F_C (Fig. 7e) maps of RA and PRDX1^{C52SC83S} (aa 1-175) are intact, indicating that the binding mode of RA in the complex structure is reliable.

The complex structure demonstrates that molecular scaffold of RA interacts with Chain A and Chain B of PRDX1, and RA binds at the peroxidatic active site of PRDX1 (Fig. 7f). Electrostatic potential map shows that the interior of RA binding site (peroxidatic site) is electronegative, whereas the exterior is electropositive (Fig. 7g). Overall, twelve hydrogen bonds between RA and PRDX1^{C52SC83S} (aa 1-175) form a hydrogen bond network, thereby stabilizing the residues in the binding site (Fig. 7h). Of particular note, RA's carboxyl group and carbonyl group form hydrogen bonds with T49 and F50 of Region I, and V51 and S52 of the C_P loop (peroxidatic cysteine-containing loop) of PRDX1 (Supplementary Fig. 8b). It has been suggested that salt-bridged hydrogen bonds formed between the peroxidatic cysteine and conserved R128 stabilize the active site and promote H_2O_2 binding[49]. Thus, hydrogen bonds between R128 and S52 bridged by RA's carboxyl group help to stabilize the peroxidatic cysteine (Supplementary Fig. 8c). Taken together, we propose that the hydrogen bond network formed between RA and the active site of PRDX1 helps to activate PRDX1's peroxidase activity.

https://doi.org/10.1038/s41467-025-55939-2

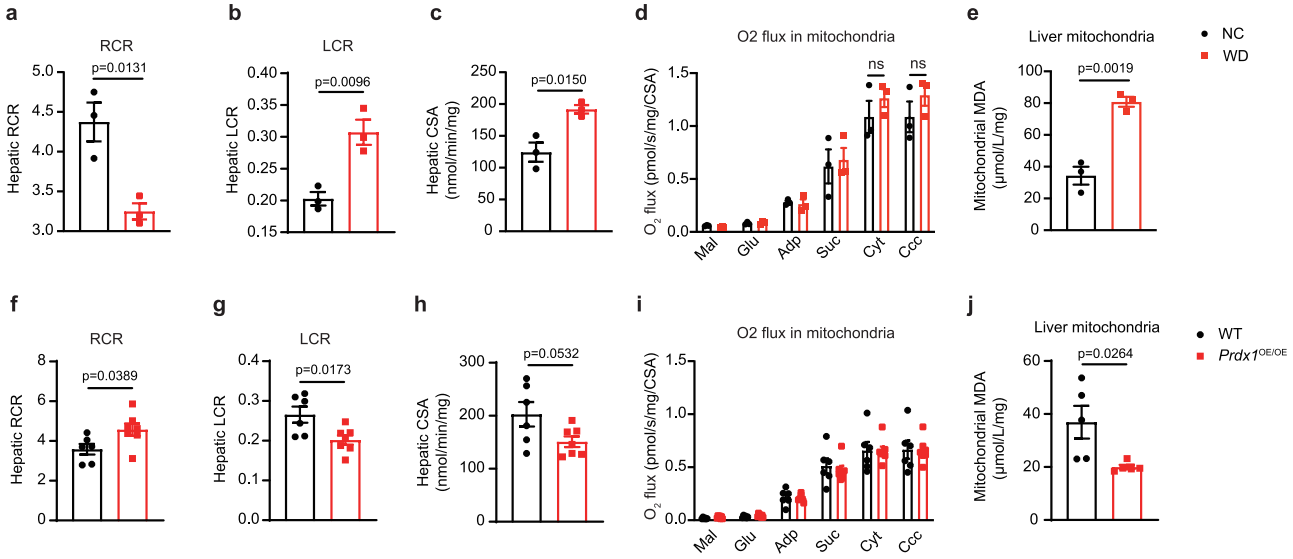

Fig. 6 | PRDX1 protects liver mitochondrial function. a Hepatic respiratory control ratio (RCR) of mice on NC or WD. 8-week-old male C57BL/6 mice were fed a NC or WD for 20 weeks before their liver mitochondria were isolated for O2k analyses. $n = 3$ mice per group. **b** Hepatic leaking control ratio (LCR) (as in a). $n = 3$ mice per group. **c** Hepatic citrate synthase activity (CSA) (as in a). $n = 3$ mice per group. **d** O_2 flux in isolated liver mitochondria (as in a). $n = 3$ mice per group; ns, no significance. Mal, malate; Glu, glutamate; Suc, succinate; Cyt, cytochrome c; Ccc, cccp. ns, no significance by unpaired Student's t test. **e** MDA concentration in the liver mitochondria isolated from mice after NC or WD (as in a). $n = 3$ mice per group. **f** Hepatic RCR of WT and *Prdx1*$^{OE/OE}$ mice. 8-week-old male WT and *Prdx1*$^{OE/OE}$ mice were fed a WD for 20 weeks before their liver mitochondria were isolated for O2k analyses. WT mice ($n = 6$); *Prdx1*$^{OE/OE}$ mice ($n = 7$). **g** Hepatic LCR (as in f). WT mice ($n = 6$); *Prdx1*$^{OE/OE}$ mice ($n = 7$). **h** Hepatic CSA (as in f). WT mice ($n = 6$); *Prdx1*$^{OE/OE}$ mice ($n = 7$). **i** O_2 flux in isolated liver mitochondria (as in f). WT mice ($n = 6$); *Prdx1*$^{OE/OE}$ mice ($n = 7$). **j** MDA concentration in the liver mitochondria isolated from WT and *Prdx1*$^{OE/OE}$ mice after WD. $n = 5$ mice per group. All the data are presented as means ± SEM. Unpaired and two-tailed Student's t test was performed for **a**–**j**.

We next validated the specificity of RA for PRDX1. RA treatment (30 min) significantly increased the peroxidase activity of global PRDX in WT HepG2 cells (Supplementary Fig. 8d); in contrast, RA treatment in PRDX1 knockout HepG2 cells had no effect on PRDX peroxidase activity (Supplementary Fig. 8e). Likewise, RA treatment in WT mice significantly increased the peroxidase activity of global hepatic PRDX (Supplementary Fig. 8f), but did not alter hepatic PRDX peroxidase activity in PRDX1 knockout mice (Supplementary Fig. 8g).

RA is a natural compound derived from plants with anti-oxidant and anti-inflammatory activities[50], and has shown hepatoprotective effects[51,52]; Consistently, RA treatment significantly inhibited IL-6-induced ROS increase (Supplementary Fig. 8h), and LPS-induced expression of pro-inflammatory cytokines (IL-6 and IL-1β) in primary mouse hepatocytes (Supplementary Fig. 8i, j). Interestingly, we found that RA dose-dependently reduced the levels of recombinant WT PRDX1 hyperoxidation in vitro (Supplementary Fig. 8k), as well as LPS-stimulated PRDX hyperoxidation in HepG2 cells (Supplementary Fig. 8l). Given that PRDX1 hyperoxidation suppresses its peroxidase activity[17], these data suggest that RA could activate PRDX1's peroxidase activity partially, if not completely, by reducing its hyperoxidation. Collectively, these results demonstrate that RA is a highly potent and specific agonist of PRDX1 with both anti-oxidant and anti-inflammatory activities.

RA treatment alleviates NASH and liver fibrosis

We next evaluated RA activity in WD-induced NASH. RA treatment significantly increased the peroxidase activity of global PRDX in the liver of WD-fed WT mice (Supplementary Fig. 9a). Although RA treatment did not change body weight, energy expenditure and locomotion activity (Supplementary Fig. 9b–d), it significantly improved glucose intolerance (Supplementary Fig. 9e) and insulin sensitivity (Supplementary Fig. 9f). In addition, RA treatment effectively reduced the levels of hepatic H_2O_2 and lipid peroxidation (Fig. 8a, b, and Supplementary Fig. 9g), and liver fibrosis as shown by the staining of Sirius Red and α-SMA (Fig. 8c), though RA treatment did not alter fat accumulation in the liver as shown by Oil Red O staining (Supplementary Fig. 9h). Consistent with these phenotypes, we observed that in RA-treated mice there was a significant reduction in the expression of numerous pro-inflammatory or fibrotic genes (e.g., *Mcp-1, Tnf-α, F4/80, Cd11b, Cd11c, Col1a1, Col3a1, Pdgfa, Pdgfra* and *Pdgfb)* (Fig. 8d), and in hepatic STAT1 and STAT3 phosphorylation (Fig. 8e). Of note, RA treatment significantly reduced the levels of PRDX hyperoxidation in the liver (Supplementary Fig. 9i). In addition, RA treatment improved the liver mitochondrial coupling and respiratory efficiency as indicated by significantly reduced LCR, but did not alter CSA levels or mitochondrial O_2 flux (Fig. 8f, g, and Supplementary Fig. 9j, k).

We also evaluated RA activity in MCD-induced NASH. RA treatment significantly increased the peroxidase activity of global PRDX in the liver of MCD-fed WT mice (Supplementary Fig. 9l). Although RA treatment did not alter fat accumulation in the liver (Supplementary Fig. 9m), it effectively reduced liver fibrosis (Fig. 8h), hepatic STAT1 and STAT3 phosphorylation (Fig. 8i), and expression of several inflammatory or fibrotic genes in the liver (e.g., *Cd11c, Col1a1, Col3a1, Pdgfb*, and *Pdgfra*) (Fig. 8j). In addition, RA treatment improved the liver mitochondrial function as revealed by significantly decreased LCR and increased O_2 flux in the liver mitochondria (Fig. 8k, l, and Supplementary Fig. 9n, o).

In contrast, RA treatment in WD-fed *Prdx1*$^{-/-}$ mice did not change hepatic H_2O_2 levels and the extent of lipid peroxidation (Supplementary Fig. 10a, b), nor mitigated NASH symptoms (Supplementary Fig. 10c) and hepatic STAT1 and STAT3 phosphorylation (Supplementary Fig. 10d). In addition, RA treatment did not improve liver mitochondria function as assessed with O2k system (Supplementary Fig. 10e–h). Together, these results indicate that RA protects against WD-induced NASH and fibrosis by specifically activating PRDX1.

Collectively, through specifically activating PRDX1's peroxidase activity and reducing hepatic H_2O_2 levels, RA treatment suppresses hepatic STAT1 and STAT3 signaling activity, protects liver mitochondrial function, and ultimately alleviates NASH and liver fibrosis.

https://doi.org/10.1038/s41467-025-55939-2

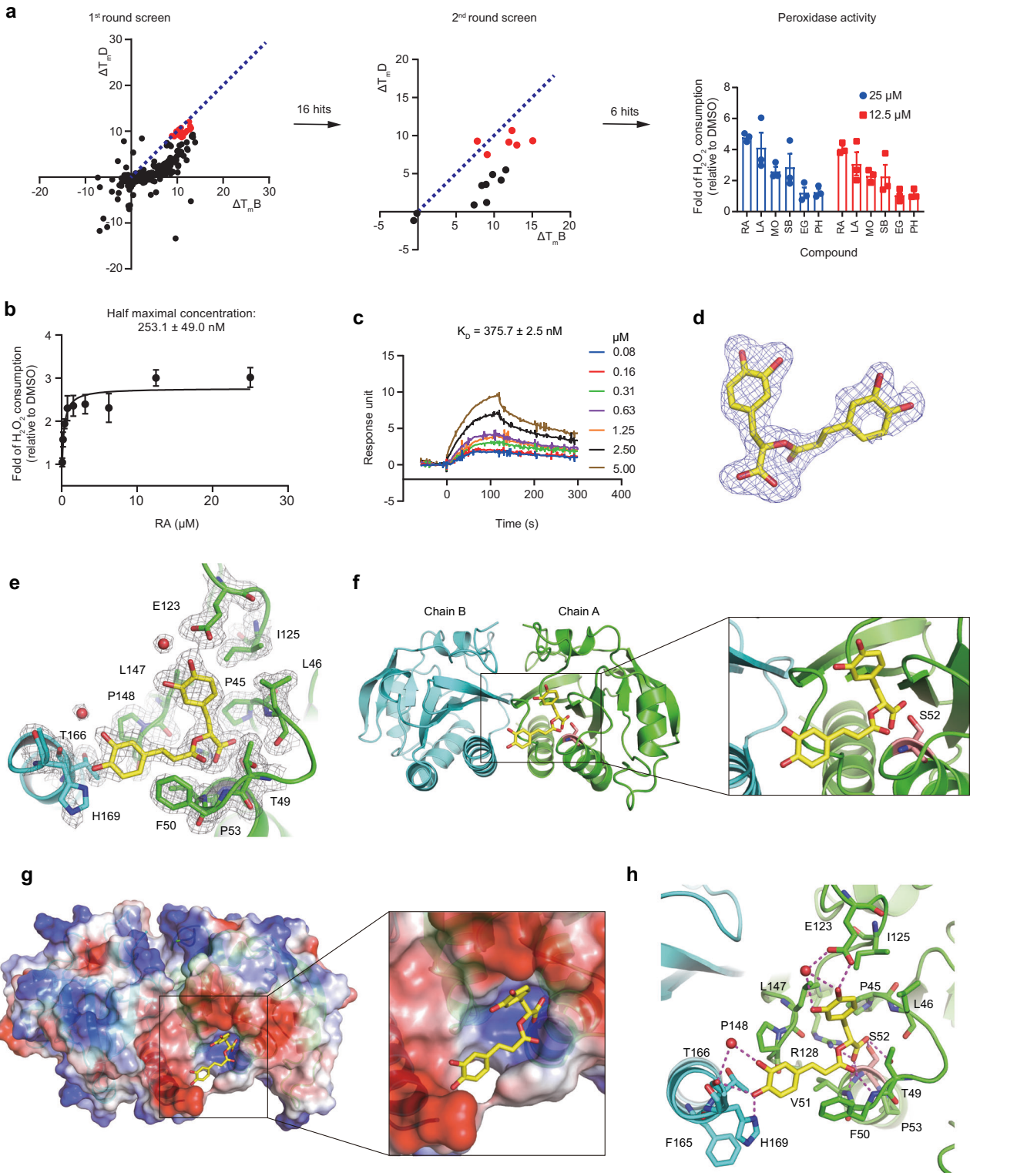

PRDX1 peroxidase dead mutant (PRDX1^{Cys52Ser}) confers resistance to NASH by increasing the Hippo pathway

PRDX1 shows both anti-oxidative (peroxidase) and pro-inflammatory (molecular chaperone) activities[24,27]. Interestingly, one previous study performed in cultured cells has implied that the peroxidatic cysteine 52 (cys52) of PRDX1 could underlie its pro-inflammatory activity[53]. To investigate whether PRDX1 cys52 mediates its pro-inflammatory activity in vivo, we recently generated a PRDX1 mutant mouse model (PRDX1^{Cys52Ser}), where PRDX1 cys52 was mutated to ser52 and consequently PRDX1's peroxidase activity was impaired[54]. Surprisingly, PRDX1^{Cys52Ser} mice showed robust resistance to diet-induced NASH[54]. These findings are potentially inconsistent with a protective role of PRDX1 against NASH through its peroxidase activity as demonstrated in this study.

We sought to understand how PRDX1^{Cys52Ser} mutant confers resistance to NASH although impairing PRDX1's peroxidase activity. We fed WT and PRDX1^{Cys52Ser} mice a CDAHFD and analyzed NASH phenotypes. Consistent with our previously observed resistance of PRDX1^{Cys52Ser} mice to either WD- or MCD-induced NASH[54], PRDX1^{Cys52Ser} mice showed significantly reduced hepatic inflammation and robust

Fig. 7 | Identification of rosmarinic acid as an agonist of PRDX1. a Identification of rosmarinic acid (RA) as a potential agonist of PRDX1. Protein thermal shift assay (PTS) was used to identify 6 hits and RA shows the highest efficacy in activating PRDX1's peroxidase activity as reflected by in vitro peroxidase activity assay. For more details, please see the Methods section. Hits are marked as red dots, while others are shown as black dots. Blue dashed lines represent the same positive values of ΔT_mD and ΔT_mB. ΔT_mD, derivative delta melting temperature; ΔT_mB, Boltzmann delta melting temperature; LA, lawsone; MO, morine; SB, Salvianolic acid B; EG, Epigallocatechin Gallate; PH, Phloracetophenone. **b** Half maximal concentration of RA for activating WT PRDX1's peroxidase activity. For **a** and **b**, data are presented as means ± SEM from three independent experiments. **c** Binding affinity of RA with WT PRDX1 by SPR assay. The dissociation constant (K_D) is shown as means ± SEM from duplicate experiments. **d** Unbiased F_O-F_C density map contoured at 2.5σ of RA in RA-PRDX1^{C52SC83S} (aa1-175) complex structure. RA is shown in yellow stick. Maps are shown in blue nets. **e** $2F_O$-F_C density map of RA and neighboring residues of PRDX1 in RA- PRDX1^{C52SC83S} (aa 1-175) complex structure. RA is shown in yellow stick. Maps are shown in gray nets. Waters are shown in red spheres. Chain A and chain B are shown in green and navy cartoon, respectively. Residues near RA are also shown as sticks. **f** Complex crystal structure showing that RA binds at the peroxidatic site of PRDX1^{C52SC83S} (aa 1-175). The peroxidatic site is highlighted in salmon stick. RA, Chain A and Chain B are shown as in (**e**). **g** Electrostatic potential of RA-PRDX1 ^{C52SC83S} (aa 1-175) complex crystal structure and RA binding site. The interior of RA's binding site is electronegative (colored in blue), while the exterior is electropositive (colored in red). **h** Hydrogen bond network formed between RA and residues in the binding pocket. Residues around 5 Å of RA are shown in stick. Waters are shown in red spheres. Hydrogen bonds are shown in magenta dashed lines.

resistance to NASH compared with WT mice after CDAHFD (Supplementary Fig. 11). Next, using immunoprecipitation (IP) combined with mass spectrometry we identified PPP1ca as a protein preferentially binding PRDX1^{Cys52Ser} over WT PRDX1 (Supplementary Fig. 12a and b), which was further confirmed by Co-IP (Supplementary Fig. 12c and d).

Numerous studies have demonstrated that as key downstream effectors of the Hippo pathway, YAP and TAZ (YAP/TAZ) stimulate NASH and liver fibrosis by promoting hepatic inflammation[55–60]. In addition, phosphorylation of YAP/TAZ leads to inhibition of their activities[55], and PPP1ca has been shown to dephosphorylate and activate TAZ[61]. These together led us to postulate that PRDX1^{Cys52Ser} mutant confers resistance to NASH by binding PPP1ca and blocking its phosphatase activity, consequently increasing TAZ phosphorylation and suppressing its activity. In line with this hypothesis, the phosphorylation levels of both PPP1ca and TAZ were significantly increased in the liver of CDAHFD-fed PRDX1^{Cys52Ser} mice (Supplementary Fig. 13a). Note that PPP1ca phosphorylation inhibits its phosphatase activity[62,63]. These results indicate that PRDX1^{Cys52Ser} mutant increases the Hippo pathway, which was also evidenced by enrichment of genes related to the Hippo pathway as revealed by RNA-Seq, and significantly decreased expression of a number of YAP/TAZ downstream genes in the liver of CDAHFD-fed PRDX1^{Cys52Ser} mice (Supplementary Fig. 13b, c). In addition, we also observed significantly reduced phosphorylation of PPP1ca and TAZ (Supplementary Fig. 14a), enrichment of genes related to the Hippo pathway (Supplementary Fig. 14b), and significantly decreased expression of several YAP/TAZ downstream genes in the liver of WD-fed PRDX1^{Cys52Ser} mice compared with WD-fed WT mice (Supplementary Fig. 14c). Taken together, these data suggest that PRDX1^{Cys52Ser} mutation increases the Hippo pathway (TAZ inhibition) by increasing PPP1ca binding and phosphorylation and consequently suppressing PPP1ca phosphatase activity, a protective effect that outweighs loss of PRDX1's peroxidase activity and ultimately reduces hepatic inflammation and ameliorates NASH.

Discussion

This study provides evidence that decreased peroxidase activity of hepatic PRDX contributes to hepatic oxidative stress and promotes NASH. Substantial evidence has demonstrated an intimate relationship between ROS and NASH[8]. Nevertheless, research attention has been mainly focused on ROS generation in the liver[64–66], especially in non-hepatocytes[67–69]. In contrast, how ROS clearance by anti-oxidants influences NASH remains poorly understood[70], although several anti-oxidants have been shown to be reduced in NASH patients[16,47]. We demonstrate that decreased global hepatic PRDX peroxidase activity accounts, at least partly, for increased hepatic H_2O_2 levels and NASH progression based on in vitro and in vivo evidence. In line with our findings, previous studies have suggested a protective role for other PRDX family enzymes including PRDX4, PRDX5 and PRDX6 against NAFLD or NASH[71–73].

Targeting NADPH oxidase to reduce ROS production is thought to be more effective in treating ROS-related vascular disease than non-enzymatic anti-oxidants such as vitamin E[74]. In this study, we show that pharmacological activation of PRDX1's peroxidase activity with RA is efficient in reducing H_2O_2 levels and improving NASH, establishing a proof of concept that boosting the peroxidase activity of PRDX1 ameliorates NASH, and indicating that PRDX1 is a promising therapeutic target. Furthermore, our study suggests that activation of anti-oxidant enzymes could be a feasible way to combat oxidative stress and related human diseases including NASH, diabetes, atherosclerosis, and cardiovascular disease.

As a common and abundant saturated FFA[75], PA displays potent lipotoxicity in NASH by inducing a variety of biological effects including inflammation and oxidative stress[35]. Indeed, we observed a significant increase of H_2O_2 levels in HepG2 cells shortly after PA treatment. Although numerous studies have uncovered the molecular mechanisms underlying PA's pro-inflammatory effects[76,77], little is known about the molecular basis of PA-induced oxidative stress. One previous study has suggested that PA stimulates oxidative stress by causing mitochondrial dysfunction and increasing ROS production from mitochondria in liver cells[64]; however, how PA causes mitochondrial dysfunction remains unclear.

Our results demonstrate that PA directly targets and inhibits the peroxidase PRDX1, providing a sound molecular basis underlying PA's lipotoxicity in stimulating oxidative stress and NASH. This regulation system could exist in NASH with or without obesity (Supplementary Fig. 15). In NASH with obesity (e.g., WD feeding), systemic insulin resistance induces lipolysis and FFA release in adipose tissue, and stimulates de novo lipogenesis in the liver[4], which inhibits PRDX1 peroxidase activity and increases H_2O_2 levels in the liver. In NASH without obesity (e.g., MCD feeding), a decrease in hepatic PRDX1 peroxidase activity could be caused by PA that is increased primarily in the liver, as increased FA uptake has been suggested to contribute to MCD-induced NASH[78]. It is also possible that PA inhibits other anti-oxidants to promote oxidative stress and NASH, given that the activities of anti-oxidant enzymes such as catalase and superoxide dismutase have been shown to be significantly reduced in NASH patients[16,47]. Thus, as a potential scenario, PA-induced lipotoxicity stimulates hepatic oxidative stress and exacerbates NASH by inhibiting the whole anti-oxidant defense system.

Our study has indicated that PRDX1 protects against NASH by scavenging H_2O_2, mitigating the oxidation of PTPs, and ultimately suppressing STAT1 and STAT3 signaling. Tiganis group has elegantly shown that the phosphorylation of distinct STAT (e.g., STAT1, STAT3 and STAT5) is significantly increased in HFD-induced NAFL or NASH, which is ascribed to the oxidation of PTPs (in particular TCPTP) caused by ROS[41,42]. They further demonstrated that STAT1 signaling accounted for NASH with obesity[42]. With regard to STAT3 signaling, previous studies have suggested that it promotes NASH and fibrosis[79,80]. Consistent with these findings, our results support that increased

https://doi.org/10.1038/s41467-025-55939-2

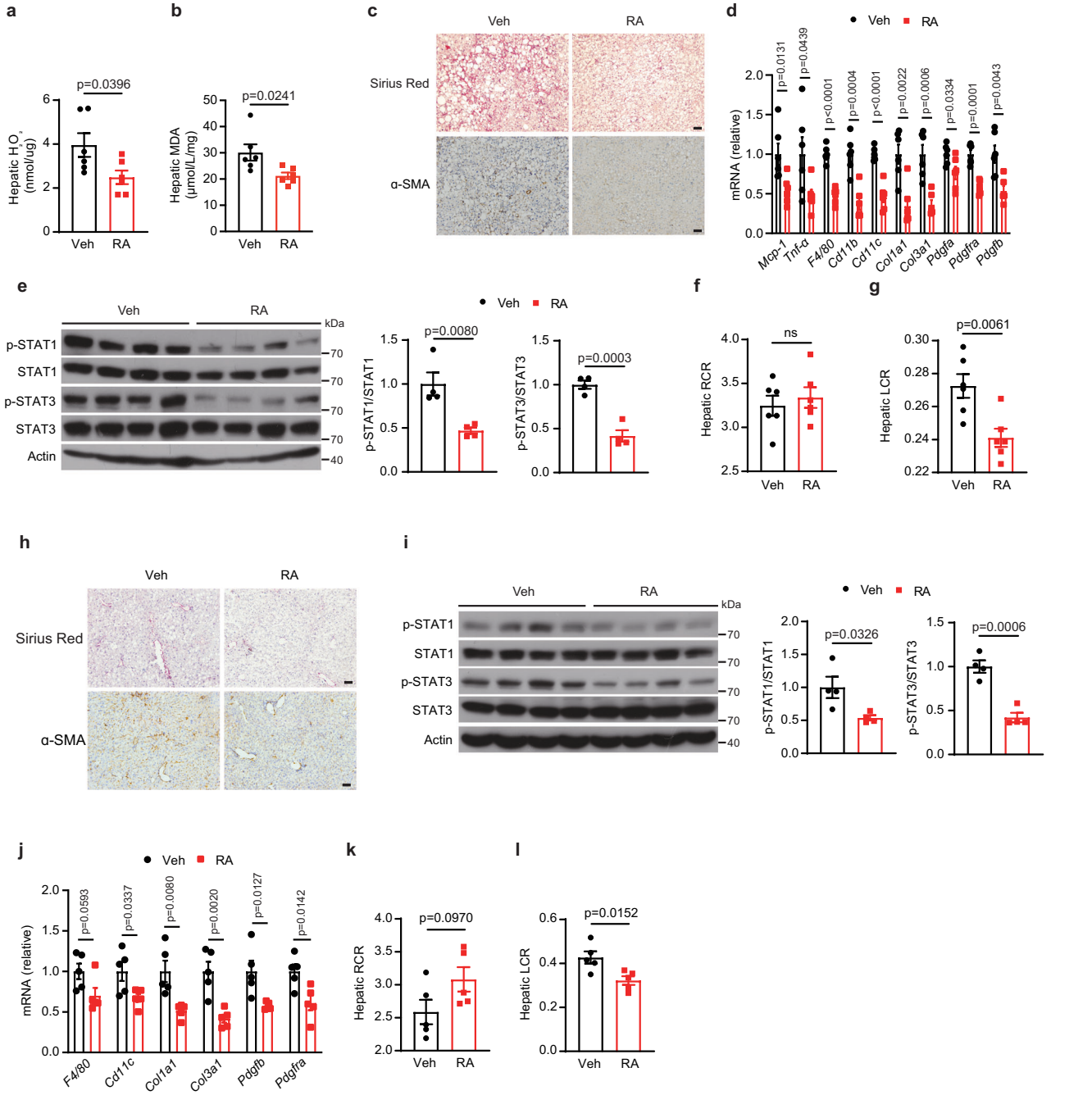

Fig. 8 | RA treatment alleviates NASH and liver fibrosis. a Hepatic H_2O_2 levels in WT mice treated with WD and RA or vehicle. 8-week-old male WT mice were fed a WD and concurrently received a daily intraperitoneal injection of either vehicle or RA (30 mg/kg) for 20 weeks. $n = 6$ mice per group. **b** Hepatic lipid peroxidation (as in a). MDA levels were measured using a lipid peroxidation MDA assay kit. $n = 6$ mice per group. **c** Representative images from three mice per group showing Sirius Red and α-SMA staining of liver (as in a). $n = 3$ biologically independent mice. Scale bars, 50 μm. **d** mRNA expression of hepatic genes (as in a). $n = 6$ mice per group. **e** Western blotting and quantitation of hepatic STAT1 and STAT3 phosphorylation (as in a). $n = 4$ mice per group. **f** Hepatic RCR. 8-week-old male WT mice were fed a WD and concurrently received a daily intraperitoneal injection of either vehicle or RA (30 mg/kg) for 20 weeks before liver mitochondria were isolated for O2k analyses. $n = 6$ mice per group. ns, no significance. **g** Hepatic LCR (as in f). $n = 6$ mice per group. **h** Representative images showing Sirius Red and α-SMA staining in the liver. 8-week-old male WT mice were fed a MCD and concurrently received a daily intraperitoneal injection of vehicle or RA (30 mg/kg) for two weeks. $n = 3$ biologically independent mice. Scale bars, 50 μm. **i** Western blotting and quantitation of hepatic STAT1 and STAT3 phosphorylation (as in h). $n = 4$ mice per group. **j** mRNA expression of hepatic genes (as in h). $n = 5$ mice per group. **k** Hepatic RCR. 8-week-old male WT mice were fed a MCD and concurrently received a daily intraperitoneal injection of vehicle or RA for two weeks before their liver mitochondria were isolated for O2k analyses. $n = 5$ mice per group. **l** Hepatic LCR (as in **k**). $n = 5$ mice per group. All the data are presented as means ± SEM. Unpaired and two-tailed Student's t test was performed for **a**–**l**, except **c** and **h**.

oxidization of PTPs and phosphorylation of STAT1 and STAT3 contribute to NASH. Our results also indicate that one common driver is H_2O_2, as H_2O_2 treatment in HepG2 cells markedly increased PTPs' oxidation and STAT1 and STAT3 phosphorylation, while PRDX1 overexpression or pharmacological activation of PRDX1 with RA significantly reduced hepatic H_2O_2 levels and hepatic STAT1 and STAT3 phosphorylation. Note that Dr. Dick group has elegantly demonstrated a redox relay between PRDX2 and STAT3, resulting in STAT3 oxidation

and inactivation[14,81]; however, whether a similar redox relay between PRDX1 and STAT1 or STAT3 that blocks their activities occurs remains unknown. In addition, how the redox relay between PRDX1 and STAT1 or STAT3 gets involved in NASH pathogenesis remains unclear, given that STAT1 activation and STAT3 activation have been shown to promote obesity-related NASH and HCC, respectively[42].

In addition to suppressing STAT signaling, PRDX1 protects liver mitochondrial function by mitigating lipid peroxidation in the liver mitochondria. Using O2k system, we found that liver mitochondria respiratory and coupling efficiency reflected by RCR or LCR was impaired in NASH mouse models, which is in agreement with one study carried out in humans[47]. Interestingly, this study also indicated that liver mitochondrial O_2 flux increases in NAFL patients with obesity but decreases in NASH patients[47], suggesting a compensatory action of liver mitochondria to counteract disease progression. Consistently, this same group recently showed that liver mitochondrial O_2 flux was significantly increased in NASH patients with obesity, whereas this enhancement was impaired in NASH patients with T2D[82]. Whether liver mitochondrial O_2 flux in NASH mouse models shows the same pattern as that in humans remains to be further defined.

It is worth noting that PRDX1 showed differential effects on body weight of mice fed a WD or MCD. PRDX1 overexpression decreased body weight of WD-fed mice by increasing their energy expenditure (Fig.4b, d), while it had no effect on body weight of MCD-fed mice (Supplementary Fig. 4d). We suppose that PRDX1 may get involved in weight control dependent of some adipokines from adipose tissue, given that WD feeding promotes considerable fat and weight gain, whereas MCD feeding causes substantial fat and weight loss. Nevertheless, more studies in future are needed to understand the molecular mechanisms behind differential weight control by PRDX1.

In summary, we demonstrate in the study that PA promotes hepatic oxidative stress and NASH by binding PRDX1 and inhibiting its peroxidase activity, and PRDX1 protects against NASH through its peroxidase activity. Hence, activation of PRDX1's peroxidase activity is a promising way to treat NASH.

Methods

Animals

All animal studies were conducted in strict accordance with the standards of animal welfare and institutional guidelines for the humane treatment of animals, and were approved by the Animal Care and Use Committee (ACUC) at Chu Hsien-I Memorial Hospital & Tianjin Institute of Endocrinology, Tianjin Medical University (DXBYY-IACUC-2020036). The mice were euthanized with CO_2 or isoflurane inhalation, followed by cervical dislocation at the end of the experiment. Male mice were used for phenotypic and mechanistic analyses throughout the study.

All mice (C57BL/6 J background) were housed at a facility with controlled temperature (22 °C), humidity and a 12/12 hr light/dark cycle, and had ad libitum access to food and water. C57BL/6 WT mice were purchased from GemPharmatech (Nanjing, China). Alb-Cre (Stock #: 003574) mouse strain was obtained from the Jackson Laboratory (Bar harbor, ME)[39]. PRDX1 KO (*Prdx1*$^{-/-}$) and overexpression (*Prdx1*$^{OE/OE}$) mice were generated by GemPharmatech (Nanjing, China) using CRISPR–cas9 approach. To generate *Prdx1*$^{-/-}$ mice, single guide RNAs (sgRNAs) targeting the exons 2–5 of Prdx1 were designed. To generate *Prdx1*$^{OE/OE}$ mice, a donor vector harboring the mouse *Prdx1* coding sequence (CDS) in fusion with an HA tag was inserted into the ubiquitous H11 site. Loxp-flanked Prdx1 (*Prdx1*$^{fl/fl}$) mouse strain was generated by GemPharmatech (Nanjing, China). To generate *Prdx1*$^{fl/fl}$ mouse strain, two loxp sequences were inserted and flanked the exon 3 (E3) of *Prdx1* gene via CRISPR-Cas9 system. PRDX1^{Cys52Ser} mice were originally generated and maintained in our laboratory[54].

Different NAFLD mouse models were induced by high-fat diet (HFD, Research Diets, D12492, 60 kcal% Fat), methionine and choline-deficient diet (MCD, MolDietes, M0421), western diet (WD, Research Diets, D09100310, 40 kcal% Fat, 20 kcal% Fructose and 2% Cholesterol), choline-deficient, amino acid-defined, HFD (CDAHFD, Research Diets, A06071302), or customized CDAHFD containing different amounts of PA (MolDietes) (Supplementary Table 3) feeding for a time as specified in the text.

Cell culture and plasmid construction

HepG2 (ATCC:HB-8065, Manassas, VA, USA) and HEK293T cells (ATCC:CRL-3216, Manassas, VA, USA) were grown at 37 °C in Dulbecco's Modified Eagle Medium (DMEM, GIBCO) supplemented with 10% fetal bovine serum (FBS, GIBCO), 100 IU/ml penicillin and 100 mg/ml streptomycin.

To examine the effects of N-Acetyl-L-cysteine (NAC, Sigma) on the phosphorylation of STAT1 and STAT3 stimulated by IL-6 (206-IL-010, R&D Systems) or IFN-γ (ab9659, Abcam), HepG2 cells were incubated with serum-free medium for 30 min, and pretreated with NAC (5 mM) for 30 min, followed by treatment with IL-6 (10 ng/ml) or IFN-γ (10 ng/ml) for another 30 min.

To assess the effect of RA on LPS-stimulated PRDX hyperoxidation (SO2/SO3), HepG2 cells were incubated with serum-free medium for 30 min, and then pretreated with RA (1 μM) for 3 hr, followed by veh or LPS (100 ng/ml) treatment for another 3 hr.

To assess the anti-inflammatory effect of RA, primary hepatocytes were isolated from 6-week-old C57BL/6 J mice as previously described[54]. The primary hepatocytes were cultured in RPMI 1640 medium containing 10% FBS for 24 hr after isolation, and then replaced with serum-free medium followed by treatment with veh, LPS (100 ng/ml) or RA (1 μM) for 6 hr.

Mutation of PRDX1 Cys52 to Ser52 (PRDX1^{Cys52Ser}) was achieved by PCR-directed mutagenesis as previously described[83]. In brief, two rounds of PCR were conducted through different pairs of primers to mutate Cys52 of PRDX1 to the Ser residue. To generate the plasmids expressing PRDX1, PRDX1^{Cys52Ser} or Ppp1ca, the mouse coding sequence (CDS) was inserted in pcDNA3.1-3xFLAG or pcDNA3.1-3xHA empty vectors (YouBio, China) with epitope fusion at the N-terminus. All DNA constructs were sequenced, and transfected in 293 T cells to confirm their protein expression before IP-MS or Co-IP analyses. All PCR primers used in the study are listed in the Supplementary Table 4.

Measurement of PRDX peroxidase activity

Global PRDX peroxidase activity in the liver or HepG2 cell lysate (freshly prepared) was measured with a classic Trx-TrxR-NADPH coupled assay as previously described[28,29] with some modifications. In brief, 200 μM NADPH (Sigma), 3 μM Trx1, and 1.5 μM TrxR1 were added in 50 mM HEPES-NaOH buffer (pH 7.0) containing 100 ug of total protein. Note that both yeast Trx1 and yeast TrxR 1 were purified by our own laboratory. 50 μM H_2O_2 was added to initiate the reaction at 30 °C, followed by detection of absorbance at 340 nm (A_{340}) every 20 s for 15 min assay duration. The background activity was simultaneously assessed without Trx and TrxR, but only with H_2O_2 and NADPH. To calculate the initial NADPH consumption rate (initial rate) (A_{340}/min/protein (g)) in the first 5 min, a smooth curve was drawn through A_{340} readings, and the initial rate was calculated by performing a simple linear regression (GraphPad Prism 9). The global PRDX peroxidase activity was calculated by subtracting the background activity (initial rate) from total activity (initial rate).

Recombinant WT PRDX1 peroxidase activity assay was conducted as previously described[84,85]. To measure the effect of sodium palmitate on recombinant WT PRDX1's peroxidase activity, recombinant WT PRDX1 (400 nM) was incubated with sodium palmitate for 30 min before addition of a mixture buffer containing 3 μM Trx, 1.5 μM TrxR, and 200 μM NADPH. NADPH reduction was monitored via A_{340} right

after the addition of 100 μM H_2O_2 for 60 min. The quantitative analysis was performed as we previously described[85]. Briefly, the slope of each assay well was calculated from linear part of the curve. The slope of assay wells without PA and PRDX1 was considered as full inhibition ($S_{100\%}$) and the slope of assay wells containing PRDX1 but no PA was considered as no inhibition ($S_{0\%}$). For PA at each concentration, the % inhibition was calculated according to the following equation: % inhibition = 100 −100 x ($S_{PA} - S_{100\%}$) / ($S_{0\%} - S_{100\%}$). The data were processed by GraphPad Prism 9.

HKPerox-Red staining in liver sections and cells

Liver samples were frozen and embedded in OCT compound (SAKURA). Cryosections were prepared at the thickness of 8 μm for HKPerox-Red staining. Frozen sections were incubated with 5 μM HKPerox-Red in PBS (0.1% DMF(Macklin), 100 mM CCl3CN (Macklin)) for 10 min at room temperature, followed by staining with DAPI (1 μg/ml) (Sigma) for 5 min. HKPerox-Red staining was performed in live cells as previously described[31]. In brief, HepG2 cells were treated with PA at different concentrations (250 μm or 500 μm) for 3 hrs, followed by incubation with HKPerox-Red (10 mM) in Hank's Buffer (0.1% DMF, 100 mM CCl3CN) at 37 °C for 30 min. Images were captured with an Olympus fluorescence microscope. To quantify the fluorescence intensity of images, Image J was used to convert RGB to 8-bit format, adjust fluorescence threshold, and measure the integrated density. Finally, the data were processed by GraphPad Prism 9.

Measurement of malondialdehyde (MDA) levels

To quantify the extents of lipid peroxidation in the liver, isolated mitochondria, or HepG2 cells, a commercial MDA detection kit (Beyotime) was applied to measure MDA concentrations according to the manufacturer's instructions. Briefly, the mixture of samples with MDA detection buffer was heated at 100 °C for 10 min, and then centrifuged at 1000 x g for 10 min at room temperature. The supernatant contained MDA-TBA adduct formed after a chemical reaction between MDA and thiobarbituric acid (TBA). MDA-TBA adduct has a maximal absorbance at 535 nm, which can be monitored by a fluorometer (BioTek). MDA concentration was finally normalized to protein concentration (mg/ml).

Physiological measurements

Measurements of weekly body weight and daily food intake were carried out as previously described[86]. Energy expenditure (kcal) and locomotion activity were monitored using Promethion High-Definition Multiplexed Respirometry System (Sable Systems, North Las Vegas, NV, USA).

Serum AST and ALT levels were analyzed with an automatic blood biochemical analyzer (AU5800, Beckman Coulter).

Histological analyses

Liver samples were fixed with 4% paraformaldehyde, embedded in paraffin and prepared for H&E, Sirius Red, or immunohistochemical staining. Staining of H&E and Sirius Red was performed with individual kits from Solarbio and Leigen companies according to the manufacturer's instructions.

Immunohistochemical staining was performed as previously described[87]. In brief, a rabbit polyclonal antibody against α-SMA (1:1000 dilution) (14395-1-AP, Proteintech) was incubated with the paraffin-fixed liver sections at 4°C overnight, followed by the incubation with a polymer-HRP anti-rabbit secondary antibody and detected with DAB (3,3′-diaminobenzidine) stain obtained from Proteintech (PK10006). An Olympus fluorescence microscope with 20x or 40x objective lens was used to capture images.

Liver samples were frozen and embedded in OCT compound (SAKURA). Cryosections were prepared at the thickness of 8 μm for Oil Red O staining as previously described[88].

Western blotting

Western blotting was performed as previously described[86]. Briefly, tissues or cultured cells were homogenized with 1 x lysis buffer containing 1% deoxycholic acid, 10 mM $Na_4P_2O_7$, 1% Triton 100, 100 mM NaCl, 5 mM EDTA, 50 mM Tris-HCl, and 0.1% SDS. Protein concentrations were determined through BCA protein assay (23228, Thermo Fisher Scientific, Rockford, IL, USA). In general, 20–40 μg of protein was loaded in SDS-PAGE and transferred to PVDF membranes. After blocking with 5% nonfat milk in TBST for 1 hr, PVDF membranes were incubated with the primary antibodies overnight at 4 °C, followed by secondary antibodies for 1 hr at room temperature (Fig. 5c–g). ECL detection systems were applied to develop signals.

To detect in vitro PRDX1 hyperoxidation (SO2/SO3), recombinant WT PRDX1 (100 ng) was incubated with RA at different concentrations for 30 min before addition of a mixture buffer containing 1.5 μM Trx, 0.8 μM TrxR, and 200 μM NADPH. The reaction was initiated with 5 μM H_2O_2. After 8 min, the reaction was quenched by 2 x sample buffer followed by SDS-PAGE and western blotting.

Antibodies

Antibodies used in this study include PRDX1 rabbit monoclonal antibody (Cell Signaling, 8499), PRDX2 rabbit polyclonal antibody (Thermo Fisher, PA5-86019), PRDX3 rabbit polyclonal antibody (Proteintech, 10664-1-AP), PRDX4 rabbit polyclonal antibody (Proteintech, 10703-1-AP), PRDX5 rabbit polyclonal antibody (Proteintech, 17724-1-AP), PRDX6 rabbit polyclonal antibody (Proteintech, 13585-1-AP), Smooth muscle actin (α-SMA) rabbit polyclonal antibody (Proteintech, 14395-1-AP), GAPDH monoclonal antibody (Proteintech, 60004-1-Ig), Oxidized PTP active site mouse monoclonal antibody (R&D Systems, MAB2844), β-Actin mouse monoclonal antibody (Sigma-Aldrich, A5441), Peroxiredoxin-SO3 rabbit polyclonal antibody (Abcam, ab16830), Phospho-STAT1 (Tyr701) (58D6) rabbit antibody (Cell Signaling, 9167), STAT1 rabbit polyclonal antibody (Cell Signaling, 9172), Phospho-STAT3 (Tyr705) (D3A7) rabbit antibody (Cell Signaling, 9145), STAT3 (D3Z2G) rabbit antibody (Cell Signaling, 12640), HA-tag (C29F4) rabbit antibody (Cell Signaling, 3724), FLAG tag rabbit antibody (Proteintech, 80010-1-RR), Phospho-STAT1 (Y701) rabbit antibody (ABclonal, AP0054), F4/80 rabbit antibody (Cell Signaling, 70076), Phospho-WWTR1(Ser89) rabbit antibody (Invitrogen, PA5-105066), PPP1ca mouse antibody (Proteintech,67070-Ig), Phospho-PPP1ca (Thr320) rabbit antibody (Proteintech, 29874-1-AP), YAP/TAZ(D24E4) rabbit antibody (Cell Signaling,8418), Goat Anti-Rabbit IgG Antibody, (H + L) HRP conjugate (Millipore, AP187P), and Goat Anti-Mouse IgG Antibody, HRP conjugate (Millipore, AP181P).

Measurement of intracellular ROS

According to the manufacturer's instructions, intracellular ROS in HepG2 cells were measured by detecting the fluorescent intensity of dichlorofluorescin (DCF), an oxidized product from non-fluorescent compound 2′,7′-dichlorodihydrofluorescein diacetate (H2DCFDA) (ThermoFisher). Briefly, HepG2 cells were starved in serum-free Hank's buffer for 30 min, followed by stimulation with PA (250 μM) for another 30 min. To evaluate the anti-oxidative effect of RA, HepG2 cells were starved in serum-free Hank's buffer and simultaneously pretreated with RA (1 μM) for 30 min, followed by stimulation with IL-6 (10 ng/ml) for another 30 min. Afterward, cells were first incubated with 5 μM H2DCFDA at 37 °C for 30 min in the darkness and then detected at 485 nm (excitation) and 520 nm (emission) by a fluorometer (BioTek).

Surface plasmon resonance (SPR)

The SPR binding assay was performed on a Biacore T200 instrument. Recombinant wild-type PRDX1 at 200 μg/ml in 10 mM sodium acetate (pH = 4.5) was coupled with the CM5 chip (GE Healthcare). After

immobilization, the system was equilibrated for 1 hr. RA was injected and flowed through the chip at a flow rate of 20 μl/ml in assay buffer with 0.05% Tween-20. As for sodium palmitate, SPR assay was performed in PBS with 0.01% NP-40. Each injection was associated with the sensor chip for 120 s and dissociated for 180 s. All data were processed using the Biacore T200 Evaluation software (version 1.0).

Cellular thermal shift assay

The cellular thermal shift was performed in HepG2 cells as previously described[36]. In brief, cells were treated with PA (Sigma) that was prepared in 10% BSA (fatty acid free, Sigma) or 10% BSA as a control for 1 hr, and then harvested and suspended in 1x PBS containing protease inhibitors (cocktail, Roche). Cell suspensions were divided into a number of aliquots (50 μl) that were heated at different temperatures ranging from 55.5 °C to 64.0 °C for 3 min, followed by cooling at room temperature for 3 min. Heated cell suspensions were freeze-thawed with liquid nitrogen for 3 times before they were centrifuged at 20,000 x *g* at 4°C for 30 min. The supernatants were collected for SDS-PAGE and western blotting analyses.

Quantitative PCR (qPCR)

qPCR was performed and quantified as previously described[86]. In brief, mouse tissues or cultured cells were homogenized in TRIzol (Invitrogen) and total RNA was extracted. In general, 1 μg RNA in total was used for reverse transcription with random primers, followed by quantitative PCR with QuantStudio 3 Real-Time PCR System (Applied Biosystems). The relative expression of target genes was calculated based on $2^{-\Delta\Delta Ct}$ method with 36b4 as the reference gene. Mouse primers used in this study were summarized in Supplementary Table 2.

IPGTT and IPITT

Intraperitoneal glucose tolerance test (IPGTT) and intraperitoneal insulin tolerance test (IPITT) were performed as previously described[86]. For IPGTT, mice were fasted overnight (16 hr) and the fasting glucose levels were measured right before mice were intraperitoneally injected with glucose (1.0 g/kg body weight). After glucose injection, blood glucose levels were measured every 30 min until 2 hr post injection. For IPITT, animals were fasted for 6 hr. The fasting glucose levels were measured before an intraperitoneal injection of insulin (1.5 U/kg body weight). Blood glucose levels were measured every 30 min until 2 hr post injection of insulin. A portable glucometer (OneTouch Ultra) was used to measure blood glucose.

Measurement of hydrogen peroxide (H_2O_2)

To measure the concentration of H_2O_2 in the liver or HepG2 cells, we employed a hydrogen peroxide assay kit (ab102500, abcam). Measurement was performed according to the manufacturer's instructions. In brief, liver or cell samples were collected fresh, washed in cold PBS, and lysed in the assay buffer. Supernatant was then subject to deproteinization to remove proteins using a commercial deproteinizing sample preparation kit (ab204708, abcam). Following protein removal, the supernatant was used for fluorometric assay at the excitation wavelength of 535 nm by a fluorometer (BioTek). H_2O_2 concentration was calculated according to the manual provided.

Generation of PRDX1 knockout HepG2 cells

To generate *PRDX1* knockout HepG2 cells, we employed CRISPR-Cas9 approach. Lentivirus (pHBLV-U6-hPrdx1-gRNA-EF1-CAS9-PURO) expressing Cas9 and gRNA for human *PRDX1* was packaged in 293 T cells by HANBIO (Shanghai, China) according to the standard procedure. HepG2 cells were infected with the packaged lentivirus and *PRDX1* knockout HepG2 cells were screened out through puromycin treatment. The knockout efficiency was confirmed by western blotting. The gRNA sequence used in this study: CCTGAGCAATGGTGCGCTTC (5′-3′).

Transcriptome analysis

Liver samples were collected from mice and stored in RNAlater (Ambion) overnight. Total RNA was isolated and purified for transcriptome analysis. In brief, RNA was isolated using TRIzol reagent and RNA quality was evaluated with Bioanalyzer 2100 (Agilent, CA, USA). With high-quality RNA, cDNA library was created and then the 2x150bp paired-end sequencing was performed on an Illumina Novaseq 6000 (LC-Bio Technology Co., Hangzhou, China).

For bioinformatics analysis, fastp software (https://github.com/OpenGene/fastp) was employed to remove unnecessary reads and verify sequence quality. HISAT2 was applied to map reads to the reference genome of mus_musculus/Ensembl/v101 and generate bam files. StringTie (https://ccb.jhu.edu/software/stringtie) was used to assemble and quantify the mapped beads of each sample with default parameters. Gffcompare (https://github.com/gpertea/gffcompare/) was used to merge all transcriptomes to reconstruct a comprehensive transcriptome, followed by estimating the expression levels of all transcripts using StringTie. R package edgeR (https://bioconductor.org/packages/release/bioc/html/edgeR.html) was used to select differentially expressed genes (DEGs). DAVID software (https://david.ncifcrf.gov/) and GSEA4.1.0 software (http://www.gsea-msigdb.org/gsea/index.jsp) was applied for Kyoto Encyclopedia of Genes and Genomes (KEGG) pathway enrichment analysis and gene-set enrichment analysis (GSEA), respectively.

Isolation of liver mitochondria

Isolation of fresh liver mitochondria for Oxygraph-2k (O2k) study was performed according to a previous study with some modifications[89]. In brief, approximately 500 mg liver tissue was collected in 2–3 ml of pre-cold mitochondria isolation buffer (225 mM mannitol (Sigma), 75 mM sucrose (Sigma), 0.2 mM EDTA (Solarbio)), followed by homogenization for 10–12 times using a Teflon-glass homogenizer. The homogenates were subject to centrifugation at 1000 x g for 10 min at 4 °C and the supernatants were collected for a second centrifugation at 6200 x g for 10 min at 4 °C. The resultant mitochondrial fraction was suspended in 1 ml of pre-cold Mir05 mitochondrial respiration medium for later O2k analyses.

The procedure for isolating liver mitochondria for MDA measurement was similar to that described above except the followings: after centrifugation at 6200 x *g* for 10 min, the pellet was lysed with 0.5 ml lysis buffer (1% Triton X-100, 0.1% SDS), followed by the centrifugation at 13,800 x *g* for 10 min at 4 °C. The supernatant was collected for measurement of MDA and protein concentration.

Assessment of mitochondrial citrate synthase activity

Mitochondrial citrate synthase activity (CSA) was measured according to a protocol from Oroboros (https://wiki.oroboros.at/index.php/MiPNet17.04_CitrateSynthase). Briefly, mitochondrial suspension was mixed with buffer (1 M Tris-HCl, 1 mM EDTA, 0.25% Triton X-100, 0.31 mM acetyl-CoA, 0.1 mM 5,5′-dithiobis (2-nitrobenzoic acid) and 0.1 M triethanolamine) and the mixture was then added with 0.5 mM oxalacetate to initiate the reaction. A spectrophotometer was applied to record the absorbance at 412 nm at 37 °C every 20 s over a 10-min period. CSA was calculated based on the following equation: $\upsilon = \frac{r_A}{l \cdot \varepsilon_B \cdot \upsilon_B} \cdot \frac{V_{cuvette}}{V_{sample} \cdot \rho}$V: specific activity of the enzyme (IU/mg protein); r_A: rate of absorbance change (dA/dt); ε_B: extinction coefficient of B (TNB) at 412 nm and pH 8.1(13.6 $mM^{-1}.cm^{-1}$); V_B: stoichiometric number of B (TNB in the reaction) ($V_B = 1$); Vcuvette: volume of solution in the cuvette; Vsample: volume of sample added to cuvette; ρ: mass concentration or density of biological material in the sample (protein concentration: mg. ml^{-1}).

Measurement of liver mitochondrial O_2 flux

We used Oxygraph-2k (O2k) (Oroboros, Austria) to assess liver mitochondrial respiration. Liver mitochondrial were isolated fresh as

described above and used for oxygen (O_2) flux measurement in Oroboros chambers containing respiration buffer (MiR05). Approximately 100 μg of total mitochondria were loaded in one chamber for every measurement. The high-resolution respirometry (HRR) protocol for measuring O_2 flux in isolated mitochondria: malate (Sigma), glutamate (Sigma), ADP (Sigma), succinate (Sigma), cytochrome c (Sigma), CCCP (Sigma). O_2 flux was monitored at different states after adding substrates or inhibitors. Hepatic mitochondrial content was determined according to CSA. Mitochondrial O_2 flux was presented as the value that was normalized to the relevant CSA.

Measurement of liver mitochondrial respiratory and coupling efficiency

As defined in one previous study[47], respiratory control ratio (RCR) and leak control ratio (LCR) was calculated as the ratio of state 3 over state o and the ratio of state o over state u, respectively. We employed O2k (Oroboros, Austria) to evaluate RCR and LCR in fresh liver mitochondria via the following protocol: malate, glutamate, ADP, succinate, oligomycin (Sigma), CCCP. Oxygen flux at different states: ADP-stimulated coupled respiration (state 3); respiration after adding oligomycin (state o), and maximal uncoupled respiration after addition of uncoupling CCCP. Approximately 100 μg of total mitochondria were loaded in one chamber for every measurement.

Compound library screening via protein thermal shift (PTS)

Polyphenolic natural compound library was purchased from TargetMol. Before screening procedures, recombinant WT PRDX1 was reduced by TCEP (Tris(2-carboxyethyl)phosphine). After reduction, PRDX1 was desalted into assay buffer (20 mM Hepes 7.0, 150 mM NaCl). Working concentration of recombinant WT PRDX1 and compounds were 10 μM and 800 μM respectively for first and second round screens. 5×SYPRO orange dye was mixed with PRDX1 and then compounds were added before melting temperature detection by QuantStudio™ 6 Flex Real-time PCR system (Applied Biosystems). The fluorescence signal was collected with gradient elevation of heating temperature from 25 °C to 95 °C for 25 min. Delta melting temperature (ΔT_mB and ΔT_mD) were calculated using assay wells containing PRDX1 without compounds as a reference with Protein Thermal Shift™ Software (version 1.2). After the first round screen, 16 compounds stood out as hits and 15 (one compound out of stock) were purchased from TargetMol or CSNPharm. All 15 hits were dissolved in DMSO at 20 mM and rescreened using the same procedure as the first round screen. Data were analyzed by GraphPad Prism 9.

Measurement of activation of PRDX1's peroxidase activity

To measure the effects of candidate compounds from library screening on PRDX1's peroxidase activity, compounds were incubated with PRDX1 (400 nM) for 0.5 hr and then mixed with pre-reaction mixture containing 1.5 μM Trx, 0.8 μM TrxR and 200 μM NADPH. The reaction was initiated with 200 μM H_2O_2 at room temperature, followed by addition of ROSGreen™ H_2O_2 probe[90–92] (MX5202, MKBio, China) in each well for H_2O_2 quantification. Activation of PRDX1's peroxidase activity by each compound was calculated from fluorescence intensity detected by ROSGreen™ H_2O_2 probe. To obtain the real fluorescence, the fluorescence intensity of assay wells containing PRDX1 and RA minus the fluorescence intensity of RA only. The delta fluorescence intensity (ΔF) was calculated as fluorescence intensity of assay wells containing pre-reaction mixture and H_2O_2 without PRDX1 and compounds (F_{blank}) minus the fluorescence intensity of assay wells containing pre-reaction mixture, H_2O_2 and PRDX1 incubation with or without compounds ($F_{PRDX1+compound}$, or $F_{PRDX1-compound}$), which reflects H_2O_2 consumption of each well ($\Delta F=F_{blank}-F_{PRDX1+compound}$, or $F_{blank}-F_{PRDX1-compound}$). To quantify the relative H_2O_2 consumption, ΔF of PRDX1 with compound was divided by that of PRDX1 without compound (fold of H_2O_2 consumption =ΔF (F_{blank} − $F_{PRDX1+compound}$) / ΔF (F_{blank} − $F_{PRDX1-compound}$). Finally, the compound's half-maximum concentration for activating peroxidase activity was calculated by GraphPad Prism 9.

Protein expression and purification

cDNAs of human WT PRDX1 protein (aa 1-199) and its truncation mutant (C52SC83S, aa 1-175) for crystallization were inserted into vector pet28a (+) with a N terminal 6× his tag and a TEV protease cleavage site. Then the constructed plasmids were transformed into *E.coli* strain BL21 (DE3). The expression of PRDX1 was induced with 400 mM IPTG at 16 °C overnight. After ultrasonication in buffer A (50 mM Tris7.0, 200 mM NaCl, 20 mM imidazole, 10 mM β-mercaptoethanol), the clear lysate was loaded into 5 ml his trap HP column (Cytiva) and eluted with 700 mM Imidazole in buffer A by AKTA Pure. The protein was desalted in assay buffer (20 mM Hepes 7.0, 150 mM NaCl) and stored at -80 °C with 5% glycerol. For crystallization, his tag was removed by TEV protease and further purified by size exclusive chromatography Superdex 75 Increase 10/300 GL (Cytiva). Protein quality was assessed with SDS-PAGE.

Crystallization, data collection and structure determination

$PRDX1^{C52SC83S}$ (aa1-175) at 5 mg/ml was crystallized in buffer (20 mM Tris 8.5, 100 mM NaCl, 1 mM TCEP) by sitting-drop method at 16 °C using a reservoir solution of 10% v/v Tacsimate pH 7.5, 0.1 M MES pH 6.5, and 25% PEG4000. Ligand free crystal was soaked in reservoir solution with the addition of 2 mM RA overnight. For data collection, the crystal was protected by cryo-protectant solution containing 25% glycerol and then flash frozen in liquid nitrogen.

X-ray diffraction data were collected at the BL19U1 beamline of National Facility for Protein Science in Shanghai (NFPS) at Shanghai Synchrotron Radiation Facility. Full 360° diffraction data were collected with a detector distance of 350 mm. The data were processed using XDS for integration and CCP4 for scale. The structure of $PRDX1^{C52SC83S}$ (aa1-175) was solved by molecular replacement using PHENIX (version 1.19.2), with the dimer of PRDX1 (PDB code: 9B7A) as the search template. RA was prepared using eLBOW module and placed using LigandFit module in PHENIX. The initial refinement was carried out in PHENIX and then checked manually in Coot (version 0.9.4). Data collection and refinement statistics are shown in Supplementary Table 1.

Administration of RA in mice

To evaluate the therapeutic potential of RA (CSNpharm) in improving NASH, RA was prepared fresh in saline and injected (30 mg/kg) once daily intraperitoneally in mice that concurrently were fed a specific diet to induce NASH.

Analysis of lipid peroxidation by liquid chromatography (LC) mass spectrometry (MS)

Lipid peroxidation analysis was performed as described[93]. Briefly, PE (D16:1) and PC (D14:1) were used as internal standards in each sample, and lipids were extracted using the Folch method. Next, 0.005% BHT in ice-cold chloroform/methanol (v/v = 2:1) was added to samples, vortexed and incubated on ice for 15 min. After centrifugation, the lower organic layers were collected in a new tube and dried under N_2 flux. The dried samples were resuspended in 60 μL of 100% LC solvent B, followed by being aliquoted and transferred to a new autosampler vial for analysis.

Mass spectrometric analysis was performed in the multiple-reaction monitoring (MRM) of specific precursor–product ion m/z transitions upon collision-induced dissociation. The precursor negative ions monitored were the molecular ions [M − H]− for PE, and the acetate adducts [M + CH3COO]− for PC. Meanwhile, identity

was verified by monitoring. The positive molecular ions [M + H]+ for both PC and PE were monitored simultaneously using polarity switching.

Immunoprecipitation (IP)-mass spectrometry (MS) and Co-IP

To identify proteins differentially interacting with WT PRDX1 and PRDX1^{Cys52Ser} mutant, pcDNA3.1-3xFlag-PRDX1 and pcDNA3.1-3xFlag-PRDX1^{Cys52Ser} expression constructs were transfected in HEK293T cells for 48 hr. Afterward, cells were harvested and lysed in 1% NP-40 lysis buffer (20 mM Tris-HCl, 0.5% NP40, 150 mM NaCl, 1 mM EDTA with complete protease inhibitor cocktail (Roche) and phosphatase inhibitor (PhosSTOP, Roche)). Cell lysates were used for immunoprecipitation (IP). Briefly, 4 mg of total protein was incubated with 50 µL of Anti-Flag M2 affinity gel (Sigma, A2220) at 4°C for overnight, followed by washing with 1x lysis buffer six times. After the final wash, the precipitated protein samples were denatured in 2xSDS sample buffer at 100 °C for 10 min, followed by SDS-PAGE and coomassie blue staining.

The subsequent proteome analysis was carried out by Jingjie Biotechnology Co. (Hangzhou, China). For in-gel tryptic digestion, coomassie blue-stained gel bands were cut and destained in 50 mM NH_4HCO_3 in 50% acetonitrile (v/v) until clear. The gel pieces were dehydrated with 100% acetonitrile for 5 min, and rehydrated in 10 mM DTT at 37 °C for 60 min. After two additional rounds of dehydration and rehydration, the gel pieces were digested with trypsin (10 ng/µl) at 37°C overnight. Peptides were extracted, and then dried to completion and resuspended in 2% acetonitrile/0.1% formic acid.

For mass spectrometry (MS) analysis, the tryptic peptides were separated by EASY-nLC 1200 UPLC system and analyzed through Orbitrap Exploris 480 MS. The MS data were processed using Proteome Discoverer 2.4.

To validate the interaction between PPP1ca and PRDX1 or PRDX1^{Cys52Ser}, plasmids expressing 3xFlag tagged protein or 3xHA tagged protein were co-transfected in 293 T cells for Co-IP analysis. 48 hr post transfection, cells were harvested for IP using Anti-Flag M2 affinity gel or normal mouse IgG magnetic beads as described above. Finally, the precipitated protein samples were analyzed by WB to investigate protein interaction.

Statistical analysis

All results are presented as means ± SEM. ImageJ was used to quantify protein levels from western blotting images, or fluorescence intensity from microscopic images. Statistical analyses were performed with unpaired and two-tailed Student's t test (Excel 2011), or one-way and two-way ANOVA followed by the Bonferroni test for multiple comparisons (GraphPad Prism 9). $p < 0.05$ was considered statistically significant. GraphPad Prism 9 and Adobe Illustrator CS 2020 were used to generate and prepare all figures.

Reporting summary

Further information on research design is available in the Nature Portfolio Reporting Summary linked to this article.

Data availability

All the data generated or analyzed in this study are included in this paper or the Supplementary Information. The RNA-Seq data generated in the study have been deposited in Gene Expression Omnibus (GEO) under accession codes GSE201030 and GSE271914. The PRDX1-RA complex structure data have been deposited in the Protein Data Bank (PDB) under accession code 9B7A. Source data are provided with this paper.

References

1. Birkenfeld, A. L. & Shulman, G. I. Nonalcoholic fatty liver disease, hepatic insulin resistance, and type 2 diabetes. *Hepatology* **59**, 713–723 (2014).
2. Younossi, Z. M. et al. Global epidemiology of nonalcoholic fatty liver disease-Meta-analytic assessment of prevalence, incidence, and outcomes. *Hepatology* **64**, 73–84 (2016).
3. Loomba, R., Friedman, S. L. & Shulman, G. I. Mechanisms and disease consequences of nonalcoholic fatty liver disease. *Cell* **184**, 2537–2564 (2021).
4. Ferguson, D. & Finck, B. N. Emerging therapeutic approaches for the treatment of NAFLD and type 2 diabetes mellitus. *Nat. Rev. Endocrinol.* **17**, 484–495 (2021).
5. Targher, G., Corey, K. E., Byrne, C. D. & Roden, M. The complex link between NAFLD and type 2 diabetes mellitus - mechanisms and treatments. *Nat. Rev. Gastroenterol. Hepatol.* **18**, 599–612 (2021).
6. Lim, J. S., Mietus-Snyder, M., Valente, A., Schwarz, J. M. & Lustig, R. H. The role of fructose in the pathogenesis of NAFLD and the metabolic syndrome. *Nat. Rev. Gastroenterol. Hepatol.* **7**, 251–264 (2010).
7. Friedman, S. L., Neuschwander-Tetri, B. A., Rinella, M. & Sanyal, A. J. Mechanisms of NAFLD development and therapeutic strategies. *Nat. Med* **24**, 908–922 (2018).
8. Musso, G., Cassader, M. & Gambino, R. Non-alcoholic steatohepatitis: emerging molecular targets and therapeutic strategies. *Nat. Rev. Drug Discov.* **15**, 249–274 (2016).
9. Chen, Z., Tian, R., She, Z., Cai, J. & Li, H. Role of oxidative stress in the pathogenesis of nonalcoholic fatty liver disease. *Free Radic. Biol. Med* **152**, 116–141 (2020).
10. Storz, P. & Toker, A. Protein kinase D mediates a stress-induced NF-kappaB activation and survival pathway. *EMBO J.* **22**, 109–120 (2003).
11. Pessayre, D. & Fromenty, B. NASH: a mitochondrial disease. *J. Hepatol.* **42**, 928–940 (2005).
12. Gandhi, C. R. Hepatic stellate cell activation and pro-fibrogenic signals. *J. Hepatol.* **67**, 1104–1105 (2017).
13. Sies, H., Berndt, C. & Jones, D. P. Oxidative Stress. *Annu Rev. Biochem* **86**, 715–748 (2017).
14. Sobotta, M. C. et al. Peroxiredoxin-2 and STAT3 form a redox relay for H2O2 signaling. *Nat. Chem. Biol.* **11**, 64–70 (2015).
15. Birben, E., Sahiner, U. M., Sackesen, C., Erzurum, S. & Kalayci, O. Oxidative stress and antioxidant defense. *World Allergy Organ J.* **5**, 9–19 (2012).
16. Videla, L. A. et al. Oxidative stress-related parameters in the liver of non-alcoholic fatty liver disease patients. *Clin. Sci. (Lond.)* **106**, 261–268 (2004).
17. Rhee, S. G. & Kil, I. S. Multiple functions and regulation of mammalian peroxiredoxins. *Annu Rev. Biochem* **86**, 749–775 (2017).
18. Perkins, A., Nelson, K. J., Parsonage, D., Poole, L. B. & Karplus, P. A. Peroxiredoxins: guardians against oxidative stress and modulators of peroxide signaling. *Trends Biochem Sci.* **40**, 435–445 (2015).
19. Winterbourn, C. C. Reconciling the chemistry and biology of reactive oxygen species. *Nat. Chem. Biol.* **4**, 278–286 (2008).
20. Cox, A. G., Winterbourn, C. C. & Hampton, M. B. Mitochondrial peroxiredoxin involvement in antioxidant defence and redox signalling. *Biochem J.* **425**, 313–325 (2009).
21. Cao, J. et al. Prdx1 inhibits tumorigenesis via regulating PTEN/AKT activity. *EMBO J.* **28**, 1505–1517 (2009).
22. Kisucka, J. et al. Peroxiredoxin1 prevents excessive endothelial activation and early atherosclerosis. *Circ. Res* **103**, 598–605 (2008).
23. He, Y. et al. Circulating Peroxiredoxin-1 is a novel damage-associated molecular pattern and aggravates acute liver injury via promoting inflammation. *Free Radic. Biol. Med* **137**, 24–36 (2019).
24. Shichita, T. et al. Peroxiredoxin family proteins are key initiators of post-ischemic inflammation in the brain. *Nat. Med* **18**, 911–917 (2012).

25. Zhang, Z. et al. Guanine nucleotide-binding protein g(i) subunit alpha 2 exacerbates nash progression by regulating peroxiredoxin 1-related inflammation and lipophagy. *Hepatology* **74**, 3110–3126 (2021).
26. Min, Y., Kim, M. J., Lee, S., Chun, E. & Lee, K. Y. Inhibition of TRAF6 ubiquitin-ligase activity by PRDX1 leads to inhibition of NFKB activation and autophagy activation. *Autophagy* **14**, 1347–1358 (2018).
27. Bae, S. H. et al. Concerted action of sulfiredoxin and peroxiredoxin I protects against alcohol-induced oxidative injury in mouse liver. *Hepatology* **53**, 945–953 (2011).
28. Kim, J. A., Park, S., Kim, K., Rhee, S. G. & Kang, S. W. Activity assay of mammalian 2-cys peroxiredoxins using yeast thioredoxin reductase system. *Anal. Biochem* **338**, 216–223 (2005).
29. Nelson K. J., Parsonage D. Measurement of peroxiredoxin activity. *Curr. Protoc. Toxicol.* **Chapter 7**, Unit7 10 (2011).
30. Bjornsson, E., Nordlinder, H. & Olsson, R. Clinical characteristics and prognostic markers in disulfiram-induced liver injury. *J. Hepatol.* **44**, 791–797 (2006).
31. Ye, S., Hu, J. J., Zhao, Q. A. & Yang, D. Fluorescent probes for in vitro and in vivo quantification of hydrogen peroxide. *Chem. Sci.* **11**, 11989–11997 (2020).
32. Woo, H. A. et al. Reversing the inactivation of peroxiredoxins caused by cysteine sulfinic acid formation. *Science* **300**, 653–656 (2003).
33. Woo, H. A. et al. Reversible oxidation of the active site cysteine of peroxiredoxins to cysteine sulfinic acid. Immunoblot detection with antibodies specific for the hyperoxidized cysteine-containing sequence. *J. Biol. Chem.* **278**, 47361–47364 (2003).
34. Font-Burgada, J., Sun, B. & Karin, M. Obesity and cancer: the oil that feeds the flame. *Cell Metab.* **23**, 48–62 (2016).
35. Marra, F. & Svegliati-Baroni, G. Lipotoxicity and the gut-liver axis in NASH pathogenesis. *J. Hepatol.* **68**, 280–295 (2018).
36. Martinez Molina, D. et al. Monitoring drug target engagement in cells and tissues using the cellular thermal shift assay. *Science* **341**, 84–87 (2013).
37. Cheng, D. et al. MGAT2 inhibitor decreases liver fibrosis and inflammation in murine NASH models and reduces body weight in human adults with obesity. *Cell Metab.* **34**, 1732–1748.e1735 (2022).
38. Benoit, S. C. et al. Palmitic acid mediates hypothalamic insulin resistance by altering PKC-theta subcellular localization in rodents. *J. Clin. Invest* **119**, 2577–2589 (2009).
39. Postic, C. et al. Dual roles for glucokinase in glucose homeostasis as determined by liver and pancreatic beta cell-specific gene knockouts using Cre recombinase. *J. Biol. Chem.* **274**, 305–315 (1999).
40. Bourdeau, A., Dube, N. & Tremblay, M. L. Cytoplasmic protein tyrosine phosphatases, regulation and function: the roles of PTP1B and TC-PTP. *Curr. Opin. Cell Biol.* **17**, 203–209 (2005).
41. Gurzov, E. N. et al. Hepatic oxidative stress promotes insulin-STAT-5 signaling and obesity by inactivating protein tyrosine phosphatase N2. *Cell Metab.* **20**, 85–102 (2014).
42. Grohmann, M. et al. Obesity drives STAT-1-dependent NASH and STAT-3-dependent HCC. *Cell* **175**, 1289–1306.e1220 (2018).
43. Regis, G., Pensa, S., Boselli, D., Novelli, F. & Poli, V. Ups and downs: the STAT1:STAT3 seesaw of Interferon and gp130 receptor signalling. *Semin Cell Dev. Biol.* **19**, 351–359 (2008).
44. Aldini, G. et al. N-Acetylcysteine as an antioxidant and disulphide breaking agent: the reasons why. *Free Radic. Res* **52**, 751–762 (2018).
45. Sun, X. et al. Neutralization of oxidized phospholipids ameliorates non-alcoholic steatohepatitis. *Cell Metab.* **31**, 189–206.e188 (2020).
46. Pafili, K. & Roden, M. Nonalcoholic fatty liver disease (NAFLD) from pathogenesis to treatment concepts in humans. *Mol. Metab.* **50**, 101122 (2021).
47. Koliaki, C. et al. Adaptation of hepatic mitochondrial function in humans with non-alcoholic fatty liver is lost in steatohepatitis. *Cell Metab.* **21**, 739–746 (2015).
48. Wang, L. et al. ALCAT1 controls mitochondrial etiology of fatty liver diseases, linking defective mitophagy to steatosis. *Hepatology* **61**, 486–496 (2015).
49. Zeida, A. et al. Catalysis of peroxide reduction by fast reacting protein thiols. *Chem. Rev.* **119**, 10829–10855 (2019).
50. Petersen, M. & Simmonds, M. S. Rosmarinic acid. *Phytochemistry* **62**, 121–125 (2003).
51. Elufioye, T. O. & Habtemariam, S. Hepatoprotective effects of rosmarinic acid: Insight into its mechanisms of action. *Biomed. Pharmacother.* **112**, 108600 (2019).
52. Kim, M. et al. Lemon balm and its constituent, rosmarinic acid, alleviate liver damage in an animal model of nonalcoholic steatohepatitis. *Nutrients* **12**, 1166 (2020).
53. Mullen, L., Hanschmann, E. M., Lillig, C. H., Herzenberg, L. A. & Ghezzi, P. Cysteine oxidation targets peroxiredoxins 1 and 2 for exosomal release through a novel mechanism of redox-dependent secretion. *Mol. Med* **21**, 98–108 (2015).
54. Bai, Z. et al. PRDX1 Cys52Ser variant alleviates nonalcoholic steatohepatitis by reducing inflammation in mice. *Mol. Metab.* **76**, 101789 (2023).
55. Ma, S., Meng, Z., Chen, R. & Guan, K. L. The hippo pathway: biology and pathophysiology. *Annu Rev. Biochem* **88**, 577–604 (2019).
56. Mooring, M. et al. Hepatocyte stress increases expression of yes-associated protein and transcriptional coactivator with pdz-binding motif in hepatocytes to promote parenchymal inflammation and fibrosis. *Hepatology* **71**, 1813–1830 (2020).
57. Song, K. et al. Yes-associated protein in kupffer cells enhances the production of proinflammatory cytokines and promotes the development of nonalcoholic steatohepatitis. *Hepatology* **72**, 72–87 (2020).
58. Wang, X. et al. Hepatocyte TAZ/WWTR1 promotes inflammation and fibrosis in nonalcoholic steatohepatitis. *Cell Metab.* **24**, 848–862 (2016).
59. Wang, X. et al. Cholesterol stabilizes TAZ in hepatocytes to promote experimental non-alcoholic steatohepatitis. *Cell Metab.* **31**, 969–986.e967 (2020).
60. Wang, X. et al. A therapeutic silencing rna targeting hepatocyte taz prevents and reverses fibrosis in nonalcoholic steatohepatitis in mice. *Hepatol. Commun.* **3**, 1221–1234 (2019).
61. Liu, C. Y. et al. PP1 cooperates with ASPP2 to dephosphorylate and activate TAZ. *J. Biol. Chem.* **286**, 5558–5566 (2011).
62. Dohadwala, M. et al. Phosphorylation and inactivation of protein phosphatase 1 by cyclin-dependent kinases. *Proc. Natl Acad. Sci. USA* **91**, 6408–6412 (1994).
63. Kwon, Y. G., Lee, S. Y., Choi, Y., Greengard, P. & Nairn, A. C. Cell cycle-dependent phosphorylation of mammalian protein phosphatase 1 by cdc2 kinase. *Proc. Natl Acad. Sci. USA* **94**, 2168–2173 (1997).
64. Li, Z., Berk, M., McIntyre, T. M., Gores, G. J. & Feldstein, A. E. The lysosomal-mitochondrial axis in free fatty acid-induced hepatic lipotoxicity. *Hepatology* **47**, 1495–1503 (2008).
65. Bettaieb, A. et al. Hepatocyte nicotinamide adenine dinucleotide phosphate reduced oxidase 4 regulates stress signaling, fibrosis, and insulin sensitivity during development of steatohepatitis in mice. *Gastroenterology* **149**, 468–480.e410 (2015).
66. Koyama, Y. & Brenner, D. A. Liver inflammation and fibrosis. *J. Clin. Invest* **127**, 55–64 (2017).
67. Bataller, R. et al. NADPH oxidase signal transduces angiotensin II in hepatic stellate cells and is critical in hepatic fibrosis. *J. Clin. Invest* **112**, 1383–1394 (2003).
68. Paik, Y. H. et al. The nicotinamide adenine dinucleotide phosphate oxidase (NOX) homologues NOX1 and NOX2/gp91(phox) mediate hepatic fibrosis in mice. *Hepatology* **53**, 1730–1741 (2011).

69. Zhao, Q. et al. Targeting mitochondria-located circRNA SCAR alleviates nash via reducing mros output. *Cell* **183**, 76–93.e22 (2020).
70. Merry, T. L. et al. Hepatocyte glutathione peroxidase-1 deficiency improves hepatic glucose metabolism and decreases steatohepatitis in mice. *Diabetologia* **59**, 2632–2644 (2016).
71. Kim, M. H. et al. Peroxiredoxin 5 ameliorates obesity-induced nonalcoholic fatty liver disease through the regulation of oxidative stress and AMP-activated protein kinase signaling. *Redox Biol.* **28**, 101315 (2020).
72. Nabeshima, A. et al. Peroxiredoxin 4 protects against nonalcoholic steatohepatitis and type 2 diabetes in a nongenetic mouse model. *Antioxid. Redox Signal* **19**, 1983–1998 (2013).
73. Lee, D. H. et al. Peroxiredoxin 6 confers protection against nonalcoholic fatty liver disease through maintaining mitochondrial function. *Antioxid. Redox Signal* **31**, 387–402 (2019).
74. Drummond, G. R., Selemidis, S., Griendling, K. K. & Sobey, C. G. Combating oxidative stress in vascular disease: NADPH oxidases as therapeutic targets. *Nat. Rev. Drug Discov.* **10**, 453–471 (2011).
75. Carta, G., Murru, E., Banni, S. & Manca, C. Palmitic acid: physiological role, metabolism and nutritional implications. *Front Physiol.* **8**, 902 (2017).
76. Hirsova, P. et al. Lipid-Induced signaling causes release of inflammatory extracellular vesicles from hepatocytes. *Gastroenterology* **150**, 956–967 (2016).
77. Palomer, X., Pizarro-Delgado, J., Barroso, E. & Vazquez-Carrera, M. Palmitic and oleic acid: the yin and yang of fatty acids in type 2 diabetes mellitus. *Trends Endocrinol. Metab.* **29**, 178–190 (2018).
78. Rinella, M. E. et al. Mechanisms of hepatic steatosis in mice fed a lipogenic methionine choline-deficient diet. *J. Lipid Res* **49**, 1068–1076 (2008).
79. Imajo, K. et al. Hyperresponsivity to low-dose endotoxin during progression to nonalcoholic steatohepatitis is regulated by leptin-mediated signaling. *Cell Metab.* **16**, 44–54 (2012).
80. Ryu, J. et al. Differential TM4SF5-mediated SIRT1 modulation and metabolic signaling in nonalcoholic steatohepatitis progression. *J. Pathol.* **253**, 55–67 (2021).
81. Talwar, D., Messens, J. & Dick, T. P. A role for annexin A2 in scaffolding the peroxiredoxin 2-STAT3 redox relay complex. *Nat. Commun.* **11**, 4512 (2020).
82. Gancheva, S. et al. Impaired Hepatic Mitochondrial Capacity in Nonalcoholic Steatohepatitis Associated With Type 2 Diabetes. *Diabetes Care* **45**, 928–937 (2022).
83. Xie, X. et al. C2 domain-containing phosphoprotein CDP138 regulates GLUT4 insertion into the plasma membrane. *Cell Metab.* **14**, 378–389 (2011).
84. Liu, C. X. et al. Adenanthin targets peroxiredoxin I and II to induce differentiation of leukemic cells. *Nat. Chem. Biol.* **8**, 486–493 (2012).
85. Xu, H. et al. Celastrol suppresses colorectal cancer via covalent targeting peroxiredoxin 1. *Signal Transduct. Target Ther.* **8**, 51 (2023).
86. Xie, X. et al. Activation of anxiogenic circuits instigates resistance to diet-induced obesity via increased energy expenditure. *Cell Metab.* **29**, 917–931.e914 (2019).
87. Mansuy-Aubert, V. et al. Imbalance between neutrophil elastase and its inhibitor alpha1-antitrypsin in obesity alters insulin sensitivity, inflammation, and energy expenditure. *Cell Metab.* **17**, 534–548 (2013).
88. Lavina, B. et al. Superoxide dismutase gene transfer reduces portal pressure in CCl4 cirrhotic rats with portal hypertension. *Gut* **58**, 118–125 (2009).
89. Edmunds, L. R. et al. Liver-specific Prkn knockout mice are more susceptible to diet-induced hepatic steatosis and insulin resistance. *Mol. Metab.* **41**, 101051 (2020).
90. Zhu, T. et al. Normal structure and function of endothecium chloroplasts maintained by zmms33-mediated lipid biosynthesis in tapetal cells are critical for anther development in maize. *Mol. Plant* **13**, 1624–1643 (2020).
91. Yang, G. et al. A multifunctional anti-inflammatory drug that can specifically target activated macrophages, massively deplete intracellular H(2)O(2), and produce large amounts CO for a highly efficient treatment of osteoarthritis. *Biomaterials* **255**, 120155 (2020).
92. Luo, X. et al. Detection of selenocysteine with a ratiometric near-infrared fluorescent probe in cells and in mice thyroid diseases model. *Anal. Chem.* **92**, 1589–1597 (2020).
93. Wang, W. et al. CD8(+) T cells regulate tumour ferroptosis during cancer immunotherapy. *Nature* **569**, 270–274 (2019).

Acknowledgements

We greatly thank Dr. Dan Yang (Westlake University, China) for providing us with the HKPerox-Red probe, and Dr. Haipeng Sun (Tianjin Medical University, China) for critical comments on this manuscript. We are grateful to the National Centre for Protein Science Shanghai (Protein Expression and Purification system) for their instrument support and technical assistance. We thank the staff from BL19U1 beamline of the National Facility for Protein Science in Shanghai (NFPS) at Shanghai Synchrotron Radiation Facility, for assistance during data collection. This work was supported by the National Key Research and Development Program of China (2019YFA0802500 to X.X. and W.J.Z., 2021ZD0203900 and 2022YFC3400500 to C.L.), the National Natural Science Foundation of China (32271202, 31971076 to X.X., U23A20108, 92253303, 81821005, 91853205 to C.L., 81903538 to H.Z., and 82104064 to H.X.), the Tianjin Municipal Science and Technology Commission (20JCJQJC00240 to X.X.), the Science and Technology Commission of Shanghai Municipality (19XD1404700 to C.L.), the project of National Multidisciplinary Innovation Team of Traditional Chinese Medicine supported by National Administration of Traditional Chinese Medicine (ZYYCXTD-202004 to C.L.), the Discipline Research Special Project of Tianjin Medical University (2024XKNFM12 to W.Y.), the R&D Program of Guangzhou National Laboratory (GZNL2023A02012 to X.X., C.L., and W.J.Z.), the Chinese Academy of Sciences (XDB0830000 to C.L.), and the Tianjin Key Medical Discipline (Specialty) Construction Project (TJYXZDXK-032A).

Author contributions

X.X. conceived, designed, and supervised the study, interpreted the data, and wrote the manuscript. C.L. designed the study and interpreted the data. W.Y. analyzed mouse phenotypes, performed O2k assay, measurement of the global PRDX peroxidase activity, RNA-sequencing data analysis, HKPerox-Red staining, histology staining, and gene expression, and wrote the methods related to O2k assay. H.X. performed the crystallization experiments, collected X-Ray diffraction data, and wrote the manuscript regarding RA identification and complex crystal structure. Z.B. performed western blotting, gene expression, RA injection in mice, and Co-IP analyses, and analyzed mouse phenotypes. Y.Z. generated the PRDX1 KO HepG2 cells, and performed IP-MS, Co-IP, and western blotting. Y.W. and B.Z. performed compound screening and in vitro biochemical assays, and wrote the relevant methods. R.L. analyzed mouse phenotypes, measured MDA levels, and performed western blotting and gene expression analyses. Z.W. and J.S. measured the peroxidase activity of PRDX, levels of ROS and H_2O_2, analyzed mouse phenotypes. H.Z. helped analyze the crystal structure. X.C. and H.Y. carried out LC-MS based measurements of liver lipid peroxidation. D.M. carried out IP-MS analysis. X.S. and L.Y. analyzed the data and prepared the figures. C.Z. and W.N. measured serum ALT and ALT levels. H.J., K.C., D.G. and W.J.Z. analyzed and interpreted the data, and discussed the experimental design.

Competing interests

The authors declare no competing interests.

Additional information

Supplementary information The online version contains supplementary material available at https://doi.org/10.1038/s41467-025-55939-2.

Correspondence and requests for materials should be addressed to Cheng Luo or Xiangyang Xie.

Peer review information *Nature Communications* thanks James Roede and the other, anonymous, reviewer(s) for their contribution to the peer review of this work. A peer review file is available.